Model Studies of Dense Water Overflows in the Faroese Channels

Alan J S Cuthbertson[1*], Peter A Davies[1], Nataliya Stashchuk[2], Vasiliy Vlasenko[2]

[1] Department of Civil Engineering, University of Dundee, Dundee DD1 4HN, UK. E-mail: a.cuthbertson@hw.ac.uk; p.a.davies@dundee.ac.uk

[3] School of Marine Science and Engineering, University of Plymouth, Drake Circus, Plymouth PL8 4AA, UK. E-mail: vasyl.vlasenko@plymouth.ac.uk; nataliya.stashchuk@plymouth.ac.uk

* Corresponding author: Current address: Institute for Infrastructure and Environment, Heriot Watt University, Edinburgh EH14 4AS, UK. Email: a.cuthbertson@hw.ac.uk. Phone: +44 131 451 8358. Fax: +44 131 451 4617.

Abstract

The overflow of dense water from the Nordic Seas through the Faroese Channel system was investigated through combined laboratory experiments and numerical simulations using the Massachusetts Institute of Technology General Circulation Model. In the experimental study, a scaled, topographic representation of the Faroe-Shetland Channel, Wyville-Thomson Basin and Ridge and Faroe Bank Channel seabed bathymetry was constructed and mounted in a rotating tank. A series of parametric experiments was conducted using dye-tracing and drogue tracking techniques to investigate deep-water overflow pathways and circulation patterns within the modelled region. In addition, the structure of the outflowing dense bottom water was investigated through density profiling along three cross-channel transects located in the Wyville-Thomson Basin and the converging, up-sloping approach to the Faroe Bank Channel. Results from the dye-tracing studies demonstrate a range of parametric conditions under which dense water overflow across the Wyville-Thomson Ridge is shown to occur, as defined by the Burger number, a non-dimensional length ratio and a dimensionless dense water volume flux parameter specified at the Faroe-Shetland Channel inlet boundary. Drogue tracking measurements reveal the complex nature of flow paths and circulations generated in the modelled topography, particularly the development of a large anti-cyclonic gyre in the Wyville-Thompson Basin and up-sloping approach to the Faroe Bank Channel, which diverts the dense water outflow from the Faroese shelf towards the Wyville-Thomson Ridge, potentially promoting dense water spillage across the ridge itself. The presence of this circulation is also indicated by associated undulations in density isopycnals across the Wyville-Thomson Basin. Numerical simulations of parametric test cases for the main outflow pathways and density structure in a similarly-scaled Faroese Channels model domain indicate excellent qualitative agreement with the experimental observations and measurements. In addition, the comparisons show that strong temporal variability in the predicted outflow

pathways and circulations have a strong influence in regulating the Faroe Bank Channel and Wyville-Thomson Ridge overflows, as well as in determining the overall response in the Faroese Channels to changes in the Faroe-Shetland Channel inlet boundary conditions.

Keywords: Faroese Channels, dense water outflows, circulations, overflows, North Atlantic, laboratory model, computational model.

1. Introduction

The south-westwards outflow of relatively cold, relatively fresh water from the Nordic Seas to the North Atlantic Ocean is known to occur partly in the surface waters along the Greenland coast and partly at depth via several overflow locations along the Greenland-Scotland Ridge (GSR) (see, for example Hansen & Østerhus, 2000; Olsen *et al*., 2008). In the eastern section of the GSR, between Iceland and Scotland, about 2.1 Sv (on average) of the overflow water entering the Wyville Thomson Basin (WTB) from the Faroe Shetland Channel (FSC) debouches into the North Atlantic via the Faroe Bank Channel (FBC). In addition, there are spatially- and temporally-intermittent flows of undiluted FSC bottom water of about 1 Sv over the Iceland-Faroe Ridge (IFR) and 0.2 to 0.3 Sv (Sherwin *et al*. 2008) over the Wyville Thomson Ridge (WTR) [see Fig. 1(a)].

The latter component is the principal focus of attention here. Observational evidence (Sherwin & Turrell, 2005; Johnson *et al*., 2010; Sherwin *et al*., 2008) indicates that the WTR overflow forms a large part of the waters occupying the upper part of the water column in the northern Rockall Trough, entering via the Ellett Gully (EG) between the Faroe Bank (FB) and the Ymir Ridge (YR) – see Fig. 1(b). The spatial distribution of transport across the WTR itself is uncertain; the overflow has been assumed previously (Murray, 1886; Saunders, 1990) to cross at the lowest, central, part of the ridge but Ellett (1998) and Sherwin & Turrell

(2005) have noted that a large component appears to cross near the Faroe Bank before being channelled to the EG.

Many uncertainties remain over the processes responsible for the leakage of flow over the WTR and the pathways taken by the overflow as it crosses the WTR and finds its way to the Rockall Trough. For example, the degree to which the barrier presented by the Faroe Bank itself and the topographic constriction at the FBC imposes retroflection and recirculation of the dense overflow water upstream of the sill remains unclear. Similarly, the roles played by hydraulic and topographical controls at the sill itself (Whitehead, 1998; Borenäs & Lundberg, 2004; Girton *et al*, 2006) in limiting the volume flux carried downstream (and thereby diverting excess FBC overflow waters across the WTR) require further attention. Finally, open questions remain on the importance of exceedance of the transport capacity (Wåhlin, 2002) of the FBC, coupled with topographically-induced departures from geostrophy in the FBC deep water overflow (Davies *et al*, 2006), in regulating and limiting the discharge over the sill and promoting spillage over the WTR.

To investigate such processes, a combined laboratory and numerical modelling study has been undertaken of the deep-water circulation and outflow characteristics in the Faroese Channels, focused on defining the parametric conditions that result in WTR spillage. In this regard, previous field studies of the FBC deep-water outflow (e.g. Lake et al., 2005; Johnson & Sanford, 1992) have indicated the presence of comparatively homogeneous (i.e. roughly constant temperature) deep- and surface water masses, separated by a permanent and well-defined pycnocline. Lake et al. (2005) and others (e.g. Borenäs and Lundberg, 2004) have thus suggested that the FBC deep-water outflow can be approximated by adopting a 1½ layer hydraulic modelling approach, whereby the deep and dynamically-inactive upper layer is assumed to have little effect on the characteristics of the deep water outflow. In other words, the surface currents generated by the inflow of warm North Atlantic waters to the Nordic

Seas are assumed to penetrate insufficiently deep to affect the deep bottom water circulation and outflow in the FBC. This assumption has been adopted in both the laboratory and numerical studies presented herein and, thus, the potential influence of surface currents is not considered in this current study.

2. The Physical System

2.1 Topographic Model of Region

The detailed seabed topography for the Faroese Channels was extracted from a bathymetric data set provided by the General Bathymetric Chart of the Oceans (GEBCO, one arc-minute grid resolution. The main region of interest for the present study considers the dense water inflow from the Norwegian Sea (Norwegian Sea Deep Water, NSDW) at the lower end of the Faroe-Shetland Channel (FSC), its expansion and topographic routing within the Wyville-Thomson Basin (WTB) and the resulting outflow pathways either (i) wholly through the up-sloping, converging approach to the Faroe-Bank Channel (FBC) threshold sill or (ii) partly across the Wyville-Thomson Ridge (WTR) and through the Ellett Gully (EG) in addition to the FBC (see Fig. 1). The detailed seabed topographic data for this region were transformed from the standard geographic coordinate system into a reoriented local Cartesian coordinate system (X, Y, Z). This was then rescaled in the horizontal (X, Y) and vertical (Z) directions by scale factors of 1:100000 and 1:3000 respectively, resulting in a vertical distortion in the seabed topography model of ~30 (see Fig. 2). This distorted model approach is in general accordance with previous experimental studies of outflows in the Faroe Bank Channel region (e.g. Davies *et al*., 2006; Cuthbertson *et al*., 2011).

2.2 Physical System

The initial, undisturbed experimental configuration is one in which the installed seabed topography is submerged within a large rectangular tank filled with a homogeneous ambient fluid of depth H and density ρ_0 which is in a state of solid body rotation about the vertical Z axis, with angular velocity $\mathbf{\Omega} = (0, 0, \Omega)$. At time $t = 0$, a dense water inflow of source and excess density ρ_1 and $(\Delta\rho)_0$ respectively [$\rho_1 = \rho_0 + (\Delta\rho)_0$], dynamic viscosity μ and initial volume flux Q_1 is introduced at the upstream end of the topographic model [FSC boundary inlet, Fig. 2, 3(b)] via a near-bed radial source manifold. From this inlet condition, defined by typical vertical h_1 and horizontal l_1 inlet flow dimensions at the entry section [see insert, Fig. 3(b)], the dense bottom water inflow is topographically-steered through the model bathymetry before spilling over a threshold sill (*i.e.* at the FBC boundary outlet, Fig. 2) and, under specific parametric conditions (see below), through the gap in the modelled Wyville-Thomson Ridge [WTR spill, Fig. 3(b)] and out through the EG outlet (Fig. 2).

3. Experiment Arrangement

3.1 Set-up and Procedure

The experimental study was conducted in a transparent-walled rectangular tank, fabricated from acrylic material with overall dimensions of 2.5 m-long × 2.2 m-wide × 0.4 m-deep, mounted on a rotating table. The scaled topographic model was constructed by defining the full scale bathymetric data at a contour level resolution $\Delta z = 30$ m. This allowed the contoured seabed topography to be represented in the model at the appropriate vertical scale (1:3000) by layering pre-cut 10 mm sheets of appropriate shape. The resulting stepped-contour topographic model of the region [see Fig. 3(a)] was installed within the rotating tank, with a waterproof grout applied to smooth out the steps between contour layers. The topographic model was then smoothed further and painted matt black to minimise reflections

and maximise contrast for dye and drogue tracking experimental measurements [see Fig. 3(b)].

The scaled model bathymetry was installed within the tank with the minimum in-channel bed elevation $z_{b,min}$ = 0 located in the centre of the WTB (as shown in Fig. 2), corresponding to the oceanic water depth $H \approx$ 1200 m at this location. Similarly, the scaled minimum bed elevations $z_{b,min}$ at the FSC inlet section, the FBC outlet section and at the depression in the WTR were modelled as $z_{b,min}$ = 70, 130 and 200 mm, respectively [corresponding to oceanic water depths H = 990, 810 and 600 m, respectively]. As the minimum bed elevation at the FBC outlet is higher than at the FSC inlet, the dense water overflow across the FBC sill is expected to be hydraulically-controlled near this location (Girton *et al.*, 2006). As a consequence, the restricting effects of this hydraulic control are expected to limit the transport capacity through the FBC (Wåhlin, 2002, Davies *et al.*, 2006), in turn influencing the behaviour of the subcritical dense water outflow layer within the WTB and FSC.

Prior to each experimental run, the rectangular tank was filled with freshwater (ρ_0 = 998 kg.m^{-3}) to a total in-channel depth of H = 0.372 m, largely submerging the modelled seabed bathymetry. The fluid was then spun-up from rest by rotating the turntable at a prescribed constant angular velocity Ω for several hours to ensure that solid body rotation had been attained (van Heijst *et al.*, 1990). Two angular velocities Ω = 0.185 s^{-1} and 0.25 s^{-1} were used in the present study [corresponding to Coriolis parameter values of f (= 2Ω) = 0.37 s^{-1} and 0.50 s^{-1}, respectively]. At the start of each run, brine solution of constant density ρ_1 (ρ_1 = 1005, 1011 and 1020 kg.m^{-3}) was pumped into a small basin immediately upstream of the FSC inlet section via a radial inlet diffuser manifold (Figs. 2, 3). This feature was designed specifically to distribute the inflow uniformly across the FSC inlet section and minimise

initial mixing between the dense and ambient fluids. The reduced gravitational acceleration g' [$= g(\rho_1 - \rho_0)/\rho_0 = g(\Delta\rho)_0/\rho_0$] values associated with the brine inflow conditions ranged from 0.068 to 0.212 m.s^{-2} (g being the gravitational acceleration = 9.81 m.s^{-2}).

Once the interface elevation of the dense bottom water layer exceeded the minimum bed elevation at the FSC inlet, a dense, bottom gravity current of brine was initiated that propagated along the descending bed topography from the FSC to the lowest point in the WTB. The thickness of the dense bottom layer gradually increased in the WTB, with the layer eventually spilling out over the FBC sill, a time after which quasi-steady outflow conditions were attained (at the initial inflow volume flux Q_1 = 0.167 l.s^{-1}). The inlet volume flux was then subsequently increased incrementally (Q_1 = 0.167 $\rightarrow$ 0.25 $\rightarrow$ 0.333 $\rightarrow$ 0.433 l.s^{-1}) at prescribed elapsed times during each experimental run, with the dense water outflow allowed to adjust to quasi-steady conditions at each Q_1 value. Parametric changes between runs were thus introduced by varying (i) the source volume flux Q_1 of dense bottom water, (ii) the density difference $(\Delta\rho)_0 = (\rho_1 - \rho_0)$ between the dense brine and ambient receiving waters and (iii) the Coriolis parameter f (= 2Ω). For all parametric conditions tested, the outflowing dense bottom layer either remained completely contained within the WTB, before spilling out freely through the FBC outlet section, or initiated a secondary outflow pathway across the WTR before passing out through the EG outlet (see Fig. 2). In both cases, the dense water overflow from the FBC and EG outlets was routed within the surrounding rectangular tank to a gravity-driven siphon arrangement at the tank outlet (Fig. 2), from where it was removed. Details of the full range of experimental conditions considered within the study are detailed in Table 1.

3.2 Measurement Techniques

Two Jai CV-M4+CL, progressive scan, monochrome, digital CCD cameras were mounted directly above the rotating tank to record dense water outflow pathways and circulation patterns in the scaled topographic model, using dye-tracing and drogue tracking techniques, respectively. For the dye-tracing runs, fluorescene was added directly to the dense source water sump prior to its supply at the FSC inlet section via the radial manifold feed. For the drogue-tracking experiments, 5 mm-diameter, cylindrical-shaped drogue particles were deployed immediately downstream of the FSC inlet section. With quasi-steady outflow conditions established, drogues of the appropriate density for the specified parametric conditions (ρ = 1005 $\rightarrow$ 1020 kg/m^3) were deployed at 30 second intervals within the dense bottom inflow layer and were subsequently tracked in their passage through the topographic system. Spatial overlap between the two CCD camera view-fields ensured that the individual drogue tracks could be accurately tracked and correlated between the two image fields. For both the dye and drogue tests, background illumination was provided by an ambient fluorescent light source. Images were captured at 24 frames per second and at a maximum resolution of 1372×1024 pixels using the *Digiflow* (Dalziel, 2008) software package.

The spatial and temporal development of the density field $\rho(x,y,z,t)$ associated with the developing bottom outflow layer was also monitored by a fixed array of high-resolution micro-conductivity probes located along three cross-channel transects (S1 – S3, Fig. 2) within the WTB and the converging, up-sloping FBC approach channel. The probes were mounted on a rigid support frame, with a motorised rack system that allowed automated simultaneous and rapid profiling of the density fields along these three transects (see Davies *et al*., 2006; Cuthbertson *et al*., 2011) throughout the duration of the experiment. This procedure allowed cross-channel variations in isopycnal elevations to be identified and measured at the three

transects, under different parametric conditions and at different elapsed times after the initiation of the flow.

4. Scaling Considerations

4.1 Dimensional Analysis

As the minimum bed elevation at the FSC inlet section was significantly lower than at the FBC outlet section, the inlet flow dimensions (l_1, h_1) of the dense bottom water layer were influenced by the hydraulically-controlled outflow conditions at the FBC outlet section. In practice, this meant that these inlet flow dimensions could not be specified directly as independent parameters, their magnitude depending on the other externally-varied source parameters (Q_1, g' and f). To resolve this problem and to determine the likely dependence of l_1 and h_1 on the other external parameters, dimensional analysis was undertaken using the following functional relationship:

$$h_1, l_1 = \phi(Q_1, g', f) \tag{1}$$

[Note that fluid viscosity μ is not included in the dimensional analysis; Reynolds numbers of the laboratory flows are assumed to be sufficiently high (see below) that viscous effects can be neglected.] Applying dimensional analysis to Eq. (1) leads to the following non-dimensional functional relationship:

$$\left(\frac{h_1 f^2}{g'}, \frac{l_1 f^2}{g'} \right) = \phi\left(\frac{Q_1 f^5}{g'^3} \right) \tag{2}$$

The behaviour of the dense bottom water outflow through the model topography can, thus, be conveniently described in terms of the non-dimensional inlet flow dimensions $h_1 f^2/g'$ and $l_1 f^2/g'$ and a non-dimensional transport parameter $Q_1^* = Q_1 f^5/g'^3$. In addition, the well-

established non-dimensional dynamical parameters describing buoyancy-driven flows in rotating systems can also be used, *viz*.

$F_1 = v_1/(g'h_1)^{1/2}$ the densimetric Froude number, (3)

$Ro_1 = v_1/(l_1 f)$ the Rossby number, and (4)

$\mathrm{Re}_1 = 4\rho_1 v_1 h_1/\mu$ the Reynolds number, (5)

where $v_1 = Q_1/A_1$ is the mean inlet velocity (A_1 being the upstream deep-water flow area defined from the FSC inlet section shape and dimensions h_1 and l_1, see below). Note that other typical dimensionless quantities such as the Burger number Bu_1 [= $Ro_1^2.F_1^{-2}$ = $g'h_1/(l_1^2 f^2)$] and the Ekman number Ek [= $(l_1/h_1).Ro_1.\mathrm{Re}_1^{-1} = \mu/(\rho_1 f h_1^2)$] are not independent dynamical parameters as they are derived directly from Re_1, F_1 and Ro_1 and the inlet length scale ratio l_1/h_1, as shown (Davies *et al*., 2006). Similarly, the non-dimensional inlet dimensions and transport parameter, derived previously from dimensional analysis, can also be re-written as follows:

$$\frac{h_1 f^2}{g'} = \left(\frac{h_1}{l_1}\right)^2 Bu_1^{-1} \tag{6}$$

$$\frac{l_1 f^2}{g'} = \left(\frac{h_1}{l_1}\right) Bu_1^{-1} \tag{7}$$

$$Q_1^* = \frac{Q_1 f^5}{g'^3} = \frac{1}{\xi}\left(\frac{h_1}{l_1}\right)^4 Bu_1^{-3} Ro_1 \tag{8}$$

where ξ (= $l_1.h_1/A_1$) is a channel cross-section shape factor (Laanearu and Davies, 2007). For the range of h_1 values attained during the experiments (see Table 1), the shape factor ξ at the FSC inlet section varied between 1.38 and 1.47. [Note that, by definition, the same relationship between shape factor ξ and h_1 should also apply at the field-scale inlet section within the FSC]. For the range of parametric conditions tested, the dynamic non-dimensional

parameters Fr_1, Ro_1 and Bu_1 were in the range $O(10^{-2})$, $O(10^{-2} - 10^{-3})$ and $O(10^{-1} - 10^{-2})$ respectively and are, thus, of the same order as values predicted for FSC and WTB field scale conditions (Girton *et al*., 2006; Mauritzen *et al*., 2005). By contrast, corresponding values of the inlet Reynolds number Re_1 were $O(10^3)$ in the scaled model and significantly lower than the oceanic bottom outflow conditions within the FSC. However, these model Re_1 values are deemed sufficiently high to assume that the dependence of outflow properties on Re_1 can be neglected.

4.1 FSC Boundary Conditions

As the deep-water oceanic overflow conditions within the FSC are geostrophically-adjusted (Borenäs & Lundberg, 2004), it is important that geostrophic-adjustment of the dense bottom water inflow within the scaled topographic model also occurs as close to the FSC inlet section as possible. This adjustment can be estimated to occur within one internal Rossby radius [= $(g'h_1/f)^{1/2}$] of the FSC inlet section (Laanearu and Lundberg, 2003), a distance which is less than 0.3 m for the full parametric range considered (Table 1). The geostrophic-adjustment of the dense bottom water inflow is, therefore, always expected to occur in the FSC region of the topographic model (Fig. 2).

5. Experimental Results

5.1 Dye Tracing Observations

Fig. 4 shows typical plan-form images of typical dense water outflow pathways obtained during the dye-tracing runs with different Burger number Bu_1 and non-dimensional transport Q_1^* conditions specified at the FSC inlet section. Note that the colour variation shown in these traces reflects non-uniformity in the illumination of the fluorescene-dyed dense bottom water by the ambient light sources. These dye-tracing tests were thus primarily conducted to

illustrate range of flow conditions under which spillage across the WTR occurs. In this regard, it is apparent that for a certain parametric range of Bu_1: Q_1^* conditions, no spillage is observed across the WTR [e.g. Fig. 4(a)], while other parametric conditions result in strong dense water overflows across the WTR [Figs. 4(c), (d)]. However, when comparing the different experimental runs in which WTR spillage occurs (see the Bu_1: Q_1^* values marked * in Table 1), the parametric dependences are not immediately obvious. It is shown that, for individual runs with fixed values of g' and f, the propensity for WTR spillage and, indeed, the magnitude of the dense water overflow generated across the WTR, increases as the dense water transport rate Q_1 increases (see Table 1).

A non-dimensional parametric classification of the tendency for WTR overflows to occur is presented in terms of the Bu_1 and Q_1^* values in Fig. 5(a). The plot appears to indicate delineation between the parametric range under which WTR spill occurs [blue crosses, Fig. 5(a)] and conditions under which no spill is observed [red circles, Fig. 5(a)]. In addition, it is apparent from Fig. 5(a) that, at lower values of Bu_1, the relative increase in the importance of rotation to stratification effects means that the conditions required for WTR spillage tend to occur at higher non-dimensional transport rates Q_1^*. It is also interesting to note the apparent shift (increase) in the Bu_1 values for the no WTR spill runs, compared with the WTR spill conditions (for otherwise fixed g' and f values). This is due to the variation in the cross-sectional dimensions (h_1, l_1) under different volumetric influxes Q_1 specified at the FSC inlet. With the inlet Burger number $Bu_1 = g'h_1/(l_1^2 f^2)$, the dimensional ratio h_1/l_1^2 (and hence non-dimensional length ratio h_1/l_1) clearly controls the magnitude of Bu_1 in any given experimental run (i.e. for fixed g' and f). It should be noted that the "non-uniformity" of the FSC inlet cross-sectional shape (i.e. non-constant shape parameter ξ value) means that the observed variation in Bu_1 as a function of ratio h_1/l_1^2 is not straightforward. Specifically, the

ratio h_1/l_1^2 initially increases then decreases with an increasing magnitude of Q_1 (and hence h_1). By comparison, for more "uniform" triangular or parabolic cross-sections, this ratio h_1/l_1^2 will always reduce as h_1 increases, although the rate of this reduction will also diminish with increasing depth h_1.

The marked parametric delineation between WTR spill and no-spill conditions is shown more clearly by plotting a regime diagram of Q_1^* versus the non-dimensional inlet length ratio h_1/l_1 [see Fig. 5(b)]. Within this figure, the vertical dashed line drawn at $h_1/l_1 = 0.181$, separating the WTR spill and no-spill conditions, clearly represents only a first approximation of this delineation, which, based on the available experimental data, is valid only up to $Q_1^* = 0.5$. Given the topographic configuration of the laboratory model, within which the minimum bed elevations at the FBC sill and WTR outlets are significantly higher than that at the FSC inlet section, it is perhaps unsurprising that such a delineation can be defined simply on the inlet length ratio h_1/l_1, as this is undoubtedly, to some extent at least, controlled by the FBC/WTR outflow conditions themselves.

Comparison between the laboratory-scale parametric conditions and full-scale conditions experienced in the FSC is also be considered within Fig. 5. For previous field surveys, it has been noted that typical oceanic values for the deep-water overflow at the FSC inlet section are $Q_1 = 2.0 – 2.5$ Sv (10^6 m^3.s^{-1}), $g' = 0.0043 – 0.006$ m.s^{-2}, $f = 1.27 \times 10^{-4}$ s^{-1}; $l_1 = 100$ km and $h_1 = 600$ m (Borenäs and Lundberg, 2004; Mauritzen *et al.*, 2005). The non-dimensional transport parameter Q_1^* can thus be found to range from 3.05×10^{-7} to 1.04×10^{-6}, with corresponding inlet Burger numbers and non-dimensional length ratios ranging from $Bu_1 = 0.022 – 0.016$ and $h_1/l_1 = 0.006$, respectively. Within the scaled, laboratory model, the corresponding magnitudes of Q_1^*, Bu_1 and h_1/l_1 are $O(10^{-2} – 10^{-4})$, $O(10^{-2} – 10^{-1})$ and $O(10^{-1})$

respectively (see Table 1 and Fig. 5). Whilst the Bu_1 values correspond in magnitude at both scales (as anticipated), discrepancies exist between the field and model scale Q_1^* and h_1/l_1 values, which arise from the vertical distortion imposed in the laboratory model. For the non-dimensional length ratio h_1/l_1, this is easily rectified by multiplying the field-scale h_1/l_1 value by the ratio of horizontal and vertical scaling factors (i.e. $10^5/3000 = 33.3$), hence yielding the adjusted field-scale length ratio $h_1/l_1 = 0.2$. For the non-dimensional flux parameter Q_1^*, the scaling discrepancy arises from the $(h_1/l_1)^4$ term in Eq. 8, which, at field and model scales, equates to $(600/10^5)^4 = 1.296 \times 10^{-9}$ and $(0.2/1.0)^4 = 1.60 \times 10^{-3}$, respectively. Thus, matching the magnitudes $Q_1^*.(l_1/h_1)^4$ at both model and field scales, a vertically-distorted, non-dimensional transport Q_1^* can be obtained from the actual FSC inlet conditions, allowing direct comparison with model-scale parametric conditions in Fig. 5. These adjusted field-scale transport parameters are estimated from $Q_1^* \times (0.2/1.0)^4/(600/10^5)^4$ to range between 0.377 and 1.284 for the corresponding Bu_1 values of 0.022 and 0.016 [see Fig. 5(a)]. While these adjusted Q_1^* values are an order of magnitude higher than the parametric conditions tested in the laboratory model, they accord well with the general trend shown by the laboratory-scale parametric conditions. Furthermore, plotting the adjusted field-scale Q_1^* values against the vertically-distorted, inlet length ratio h_1/l_1 (= 0.2) [see Fig. 5(b)], it is clear from these parametric considerations that such oceanic values of the Norwegian Sea Deep Water (NSDW) inflow measured at the FSC inlet would be expected to result in spillage across the WTR.

5.2 Drogue-Tracking Observations

Drogue tracking runs were conducted in steady-state, dense-water outflows, as defined by specific Q_1^*: Bu_1 parametric conditions at the upstream FSC boundary (see Table 1). These steady-state conditions allowed neutrally-buoyant drogues to be added at 30 second intervals

to the dense bottom water layer immediately downstream of the FSC inlet section. This procedure ensured that each individual drogue could be tracked easily during its passage through the topographic system. Fig. 6 shows a number of drogue tracking outputs, both for an experiment run under which no WTR spill occurred [e.g. Fig. 6(a),(b)] and corresponding runs in which WTR spill did occur [e.g. Fig. 6(c)–(f)]. The time interval between individual drogue positions shown in the plots is Δt = 0.42s (i.e. equivalent to every 10^{th} image frame at 24 fps). (Note: a corresponding velocity scale cannot be determined as the vertical position of the individual drogues in the lower dense water layer is uncertain).

Immediately downstream from the FSC inlet, the majority of released drogues follow similar paths along the Faroese shelf edge, with a few also showing the influence of small scale vorticity in the dense outflow layer towards the bottom of the FSC [Figs. 6(a),(c),(d)]. Subsequently, in the vicinity of the 90° turn in channel orientation (to the right) and channel constriction at the transition between the FSC and WTB, a large proportion of the drogues follow paths on the right hand side of the outflow layer (looking downstream), as would be expected for geostrophically-adjusted dense water outflow conditions. It is noted, however, that some drogue paths are influenced by eddies forming on the left side of the channel immediately prior to this constriction [see Figs. 6(b),(f)–(h)]. Once past the constriction, many of the drogue tracks tend to deviate (to a lesser or greater degree) away from the right hand side of the outflow, with many paths deflected significantly to the left in the widening WTB section. These diversions result in a number of drogues following outflow pathways to the FBC along the left side of the WTB (*i.e*. adjacent to the WTR) and in the converging, up-sloping approach to the FBC outlet, while others are shown to be transported across the WTR in the dense water overflow [Figs. 6(c),(d)]. It is unclear whether these deflected drogue paths represent a persistent characteristic of the dense water outflow structure (i.e. general anti-

cyclonic circulation) within the WTB/FBC approach for all parametric conditions tested. [Note: Fig. 6(e) shows little evidence of these deflected pathways, with the outflowing drogues remaining on the FP side of the channel]. Analysis of further drogue tracks in the WTB/FBC approach channel (Fig. 7) also reveals the presence of strongly deflected drogue paths in this region. One drogue, in particular [see Fig. 7(b)], is shown to become trapped in an anti-cyclonic eddy at the entrance to FBC approach channel. The evidence presented from these drogue tracks appears to indicate the presence of large-scale, anti-cyclonic eddy or closed circulation (gyre) in the WTB/FBC approach channel, at least on an intermittent basis. This feature is shown to affect significantly the deep-water flow paths within the WTB by deflecting the dense water overflow layer southwards towards the WTR and potentially promoting spillage across the WTR. A schematic representation of the main outflow pathways in the WTB/FBC/WTR region is assembled from these recorded drogue tracks (Fig. 8), showing the approximate regions within the topographic model where positive and negative vorticity regions (or circulations) were observed. Direct comparisons between these experimental observations and the MITgcm numerical predictions of similar flow pathways and closed circulations within the FBC/WTB topography are discussed in detail in sections 7 and 8 of the paper.

5.3 Density Measurements

Time series density profiling data was obtained at three cross-channel transects (S1 – S3, Fig. 2) within the WTB and the up-sloping, converging approach to the FBC, allowing the dynamic evolution of the dense outflowing bottom water layer to be observed throughout each experimental run. From these density data, time-averaged isopycnal elevations [defined by the density excess contours $\rho' = (\rho - \rho_0)/(\rho_1 - \rho_0) = 0.1 \rightarrow 0.9$] could be plotted along each transect for the quasi-steady-state outflow conditions that were developed in the

modelled channel bathymetry under each parametric condition (Table 1). Fig. 9 shows typical isopycnal elevations measured along transects S1, S2 and S3 for runs with different Burger numbers Bu_1 and discharge parameter Q_1^* values, for the range of parametric conditions (Q_1, g', f) considered (see Table 1).

Two interesting features from the cross-sectional isopycnal elevation plots along transects S1 and S2 are observed (Fig. 9), specifically: (i) an undulating variability in isopycnal elevation with cross-channel distance, with isopycnal lifting and sinking observed at different measurement locations along the transect, and (ii) the "pinching" of isopycnals on the left (WTR) side of the basin. The undulations in the isopycnal structure are more apparent on transect S1 and for parametric runs at lower Q_1 values [i.e. isopycnal group (ii) at transect S1 – Figs. 9(a) and (b)], tending to diminish somewhat in the along-channel direction and for runs at higher Q_1 values [i.e. isopycnal group (i) at transect S2 – Figs. 9(a) and (b)]. However, it is noted that this property of the isopycnal field remains a distinct feature at transect S1 for all parametric conditions tested and is attributed to the presence of the closed circulation forming at the entrance to the converging, up-sloping approach to the FBC, which transect S1 is shown to intercept (see Section 8).

It is also noted from the density measurements along transect S1 that the upper boundary of the dense outflowing water layer displays a general tilt towards the left (WTR) side of the basin, especially for runs conducted under higher Q_1 conditions [i.e. isopycnal group (i) at transect S1 – Figs. 9(a) and (b)]. This inclination may be attributed partly to the parametric influence of background rotation Ω in the geostrophic adjustment of the bottom outflowing layer and/or the initiation of dense water spillage across the WTR under higher Q_1 conditions, acting to control isopycnal elevations at the WTR side of transect S1 (note: this transect is

located immediately downstream of the region of minimum bed elevation along the WTR where the dense water spillage occurs – see Fig. 2).

In comparison to the relatively complex isopycnal structure observed along transects S1 (and, to a lesser extent) S2, the corresponding density measurements obtained along transect S3 indicate the development of a sharp pycnocline, with no indication of a wedge-type distribution of isopycnals across the transect. The degree of inclination observed in these isopycnal distributions (downwards to the FB side of the channel, see Fig. 3) is controlled by geostrophic adjustment in the outflowing bottom layer along the up-sloping, converging FBC approach channel. Direct comparison between the two isopycnal groups [(i) and (ii)] shown in the separate S3 transect plots of Figs. 9(a) and (b) indicates that, for otherwise identical parametric conditions (stratification g' and rotation $f = 2\Omega$), the pycnocline is inclined to a greater degree for larger Q_1^* values (*i.e.* through a larger specified initial volume flux Q_1 at the FSC inlet boundary). In addition, comparison between equivalent S3 isopycnal groups [(i) or (ii)] in Fig. 9(a) and 9(b), also indicates that increased pycnocline tilt is also achieved by a reduction in the inlet Burger number Bu_1 (*i.e.* by reducing g' at the inlet, for otherwise equivalent parametric conditions). A similar parametric dependence is displayed for isopycnal tilt from changing the background rotation rate Ω (i.e. an increase in $f = 2\Omega$, resulting in a reduction in Bu_1, leads to an increasing pycnocline tilt in the FBC approach channel). In this sense, these parametric dependences of g' and f are in accord with those expected for geostrophically-balanced outflows, where the cross-channel geostrophic slope α_g of a sharp pycnocline forming between the dense outflow layer and upper ambient layer can be approximated by $\alpha_g \approx v_1.f/g'$ (where v_1 is the average streamwise velocity in the dense outflowing layer). Hence, an increase in either outflow velocity (i.e. through Q_1) or background rotation (i.e. through f), and/or a reduction in density stratification (i.e. through

g') is therefore expected to increase the cross-channel inclination of the pycnocline along the converging, up-sloping channel. Similar geostrophic dependencies were also demonstrated in laboratory experiments of dense water overflows in simpler rotating, up-sloping and converging channel topographies (Cuthbertson *et al*., 2011; 2013).

6. MITgcm Numerical Model

6.1 Model Set-up

Numerical simulations of the deep water outflow pathways and circulations within the Faroese Channels were conducted within a similar restricted model domain to that used in the scaled laboratory model (Fig. 2). In order to facilitate direct comparison with experimental measurements, the numerical simulations were conducted for the same vertically-distorted, scaled seabed topography as adopted for the laboratory model. Consequently, the numerical model domain had overall dimensions $L_x \times L_y \times L_z$ = 2.5 m × 2.2 m × 0.4 m, where L_x, L_y and L_z represent the scaled lengths of the NW/SE, NE/SW and vertical directions, respectively. As with the scaled, physical model, this numerical model domain orientation was chosen to ensure the incoming dense water from the FSC is constrained at the inlet boundary by the natural topographic barriers presented by the Scotland and Faroe shelves. Similarly, the outlet model boundaries at the FBC and EG were also constrained by the FP/FB and FB/YR topography, respectively (see Fig. 1).

Prediction of the dense outflow dynamics within the scaled topographic model was conducted using the Massachusetts Institute of Technology General Circulation Model (MITgcm) (Marshall *et al*., 1997). The model uses a Cartesian system of coordinates 0*xyz*, with the 0*xy* plane parallel to the undisturbed free surface and the 0*z* axis directed vertically upward. The 0*x* and 0*y* axis are directed along the boundaries of the model domain (Fig. 2). The numerical

simulations were conducted on a fine-resolution grid with horizontal steps $\Delta x = \Delta y = 0.025$ m and a vertical step $\Delta z = 0.005$ m. The coefficients of horizontal and vertical viscosity and diffusivity were taken typical for a laminar range of fluid flows, i.e. 10^{-6} m^2s^{-1}.

The methodology for running the numerical simulations is described in detail in Stashchuk *et al*. (2010, 2011). At the "cold-start" initiation time ($t = 0$) for each run, a lock gate at the FSC inlet boundary was removed and an inflow of dense bottom water of prescribed density was forced into the numerical model domain by the generated pressure gradient, with a typical inflow velocity of 0.15 ms^{-1}. The inlet lower layer depth h_1 and velocity v_1 (hence volume flux Q_1) were set constant throughout the whole run time (700 s, typically), with their prescribed magnitudes set for the specific parametric conditions under investigation (see Table 1). Orlanski-type boundary conditions (Orlanski, 1976) were specified along the other three boundaries of the model domain, while the flow at the bottom satisfied a non-slip boundary condition.

The resulting outflow pathways for the propagation of dense water through the model domain is visualised through an extra equation for passive tracer transport. A tracer concentration of $\tau = 1$ is prescribed for pure, undiluted dense bottom water, decreasing from $\tau = 1$ to 0 across the pycnocline separating the bottom gravity current from the overlying ambient water mass.

6.2 Details of Parametric Model Runs

A total of five experimental runs were simulated using MITgcm (Runs 2b, 3c, 5b, 6b and 6c – Table 1). This allowed the model sensitivity to different parametric conditions (defined by Bu_1 = 0.363, 0.202, 0.199, 0.110 and 0.114; and Q_1^* = 0.19×10^{-3}, 1.26×10^{-3}, 0.87×10^{-3}, 4.49×10^{-3} and 5.99×10^{-3}, respectively) to be investigated. For each numerical simulation, the

evolution and development of the outflowing dense water layer within the scaled model domain was simulated over a total duration of 700 s, allowing quasi-steady state outflow pathways and circulations to be established within the modelled topography. For each set of parametric conditions modelled, the generated pathways and circulations were characterised within the Faroese Channel domain through (i) simulated passive dye tracing, (ii) modelled *xy* velocity vector fields and drogue tracks and (iii) predicted density fields.

6.3 Model Comparisons with Experiments

Due to the complex nature of the dense water outflow within the topographic region under consideration, direct comparisons between experimental data and numerical simulations were largely limited to qualitative observations, with emphasis placed on modelling accurately (i) the scaled, FSC inlet parametric boundary conditions; (ii) the development of quasi-steady-state dense water outflow pathways and circulations within the FSC/WTB/FBC topography; and (iii) the conditions under which spill and no-spill occur across the WTR. In particular, the modelled dense water outflow conditions achieved at the end of each simulation were compared with (i) experimentally-observed dye traces for dense water outflow pathways and the parametric conditions for spillage across the WTR (Figs. 4 and 5); (ii) general observations on deep-water circulations established from drogue tracking experiments (Figs. 6–7); and (iii) density field measurements obtained at the transect S1 in the WTB (Fig. 9).

Fig. 10(a)–(c) show MITgcm-predicted dye traces (left images) in the lower outflowing layer for a range of parametric conditions (Runs 2b, 3c and 5b – Table 1) and corresponding experimental dye traces (right images) measured under the same parametric inlet conditions (i.e. Bu_1 and Q_1^* values). In all cases, the simulated passive dye traces show excellent agreement with the corresponding experimental observations, especially with regards to the

parametric conditions under which the initiation of dense water spillage across the WTR occurs [e.g. Bu_1: Q_1^* = 0.202: 1.26×10^{-3} (Run 2c), Fig. 10(b)]. In addition, both experimental and numerical dye traces show qualitatively similar outflow pathways through the FBC for parametric conditions under which no WTR spill occurs [e.g. Bu_1: Q_1^* = 0.363: 0.19×10^{-3} (Run 3b) and 0.199: 0.87×10^{-3} (Run 6b), Figs. 11(a) and (c), respectively]. In this sense, the numerical dye simulations appear to reinforce the proposed parametric relationships between the Q_1^*, Bu_1 and h_1/l_1 (see Fig. 5), delineating the range of deep water overflow conditions where WTR spillage is expected to occur.

Fig. 11 shows MITgcm-predicted *xy* velocity vector fields computed after 500 s at two depths (i.e. 20cm and 25cm beneath the free surface boundary) for all parametric conditions tested. These velocity fields demonstrate clearly the effect of the Coriolis force on the dense water outflow entering the scaled Faroese Channel model domain, with the boundary current (particularly evident at 25 cm depth) shown to follow the Faroese shelf edge as it propagates from the FSC through the 90° converging transition into the WTB. Some evidence of cyclonic and anti-cyclonic eddy formation is observed in the FSC at 20 cm depths [Figs. 12(a), (c) and (e)] but these appear largely absent at 25 cm. Within the WTB, the deep water outflow is shown to detach from the FP side of the basin and appears to be deflected towards the WTR, with spillage across the WTR (evident in 20 cm depth plots, Fig. 11). This detachment and deflection towards the WTR is, evidently, the result of a flow separation process associated with the generation of a large anti-cyclonic eddy in the WTB and converging approach to the FBC (most evident in the 20 cm depth plots, Fig. 11), which is also shown to influence strongly the pathways for FBC overflows (i.e. continuing to flow along the WTR and FB before spilling out through the FBC). In contrast, the presence of this large anti-cyclonic eddy decreases at greater depths (i.e. 25 cm plots, Fig. 11), with the

resulting outflow pathways towards the FBC showing lesser influence from flow separation and circulations in the WTB/FBC approach channel (*i.e.* flowing through the WTB in paths closer to the FP). Overall, these simulated velocity fields are in good qualitative agreement with observed bottom water circulations, as indicated by the experimental drogue track measurements (see Figs. 6–7). Indeed, these experimental and numerical runs indicate that observed and predicted cyclonic and anti-cyclonic circulations occur at approximately the same *xy* locations within the lower dense water layer and have similar influence on the outflow pathways to the FBC and across the WTR. In addition, comparing the MITgcm predictions for the different parametric conditions tested, the runs conducted with lower inlet Q_1 values [i.e. Runs 2b, 5b and 6b; Figs. 12(a), (c) and (e), respectively] generate more significant eddy motions at 20 cm depths than runs with higher inlet Q_1 values [i.e. Runs 3c and 6c; Figs. 12(b) and (d), respectively]. The main reason for this behaviour is that increased eddy circulations are generated closer to the pycnocline, between the dense outflowing bottom waters and the overlying ambient fluid, than at greater depths within the lower layer. In the experiments it was not possible to ascertain individual drogue elevations within the outflowing dense water layer, so that the recorded variability in observed drogue paths under the same parametric conditions may have arisen from variability in drogue elevations relative to the pycnocline. Indeed, comparing the measured drogue trajectories in Figs. 6(e) and 6(f) with the predicted velocity vector fields in Fig. 11(d) (*i.e.* under the same parametric conditions) shows that the drogues released in Fig. 6(e) may have tracked the outflowing layer at an elevation similar to the 25cm depth velocity vector plot [Fig. 11(d)]. By contrast, the drogue tracks in Fig. 6(f) appear to be more qualitatively similar to the 20cm depth velocity vector plot [Fig. 11(d)] and may be more representative of lower layer drogue trajectories close to the pycnocline.

Fig. 12 shows the evolution of the MITgcm-predicted density field across the WTB transect at the location corresponding to the lowest elevation along the WTR (see Fig. 2). The parametric simulations shown correspond to relatively moderate values of the controlling parameters, with Bu_1: Q_1^* = 0.110: 0.00449 (Run 5b) and 0.114: 0.00599 (Run 5c) in Figs. 12(a) and (b), respectively. Both test simulations reveal the process of evolution within the cross channel structure of the density field during the first 700 sec after the lock release at the FSC inlet boundary. It is observed clearly that, as for the laboratory experiments along transect S1 (Fig. 9), the isopycnal surfaces are generally tilted towards the left (WTR) side of the basin. This inclination is greatest in the beginning of the experiment when the dense water begins initially to fill the basin [i.e. at t = 150 s, Figs. 12(a) and (b)] and remains visible at the end of the adjustment period (i.e. at t = 700 s) when substantial dense water spillage is observed across the WTR. In the corresponding experimental runs, the measured pycnocline was shown generally to remain relatively sharp between the dense outflowing water and overlying ambient water layers, except in regions were strong anti-cyclonic circulations were generated at the entrance to the converging, up-sloping approach to the FBC (e.g. transect S1, Fig. 9). This particular feature of isopycnal divergence is discussed in Section 8 below.

8. Summary and Conclusions

A combined experimental and numerical study has been conducted to improve understanding of the mesoscale dynamics and structure of the Norwegian Sea Deep Water (NSDW) through the Faroese Channels and the conditions under which spillage across the Wyville-Thomson Ridge (WTR) can occur. The laboratory experiments and MITgcm numerical simulations were conducted in equivalently-scaled, vertically-distorted representations of the seabed topography in the region of interest. Both experimental observations and numerical predictions indicated that the majority of dense water originating in the Faroe-Shetland

Channel (FSC) propagated towards the Faroe Bank Channel (FBC) as the main outflow pathway. However, a range of parametric conditions were also replicated where an additional outflow pathway was initiated through the depression in the WTR, with this dense water overflow propagating subsequently down through the Ellett Gully. Dimensional analysis revealed that three non-dimensional parameters, namely the Burger number Bu_1, a volume flux parameter Q_1^* and the deep water inflow length ratio h_1/l_1, specified at the inlet boundary within the Faroe-Shetland Channel (FSC), act as controlling variables determining whether secondary overflow across the WTR is initiated. Both experimental observations and numerical simulations of passive dye tracing within the lower outflowing layer are in accord with the proposed Q_1^*: Bu_1 and Q_1^*: h_1/l_1 regime plots for WTR spill and no-spill conditions. Furthermore, the fact that the inlet volume flux Q_1 appears to play the most significant parametric role in the initiation of dense water spillage across the WTR suggests that the topographic constriction and hydraulic control imposed at the FBC outlet sill may act to limit the volume flux passing through the FBC, in turn controlling the dimensions (h_1, l_1) of the inflowing dense water layer at the FSC inlet.

One of the key features of both the experimental observations and numerical simulations is the generation of cyclonic and anti-cyclonic eddies and gyres within the Faroese Channels. These features have been shown to have a significant influence on dense water outflow pathways as well as in promoting spillage across the WTR. The formation of these flow re-circulations (and the large anti-cyclonic eddy generated upstream of the FBC in particular) are associated clearly with effects of geostrophic adjustment within the outflowing bottom layer (Pratt *et al.*, 2000). However, these also appear to be accentuated by the topographic constriction associated with the up-sloping, converging channel approach to the FBC sill, imposing retroflection and recirculation in the dense water overflow layer. This mechanism,

in turn, appears to have a strong regulatory influence on the outflow flux through the FBC. Evidence of similar cyclonic and anti-cyclonic eddies have been inferred previously through observational evidence gathered during field surveys in the region (Hansen and Østerhus, 2000; Sherwin *et al.*, 2006). The current studies also demonstrate that observed flow intrusions and separations associated with these circulations can lead to different dense water outflow pathways through the Wyville-Thomson Basin (WTB) [*i.e*. on the Faroe Plateau (FP) and Wyville-Thomson Ridge (WTR) sides of the basin (see Fig. 8). This behaviour is in accord with the "meandering plume" description of the deep-water outflow in this region, as measured by Mauritzen *et al.* (2005). Indeed, the current experimental and numerical evidence suggests that these different outflow pathways through the WTB/FBC channel approach may occur at different elevations within the dense bottom layer, depending on proximity to the pycnocline.

The influence on dense water outflow pathways from any scale-induced factors arising from the vertically-distorted, scaled model topography used in both current experimental and numerical studies is largely discounted by comparing results with the recent full-scale numerical model simulations of the Faroese Channels by Stashchuk *et al*. (2011). Good qualitative agreement is observed in the structure of the deep-water flows obtained at both scales, particularly in relation to the generation of anti-cyclonic circulation upstream of the FBC and its influence on the resulting FBC and WTR overflows. The full-scale model simulations by Stashchuk *et al*. (2011) also revealed a strong temporal variability in the predicted velocity fields following removal of the imposed lock at the FSC inlet boundary, as the incoming dense water fills the modelled Faroese Channel domain (see Fig. 4, Stashchuk *et al*., 2011). Indeed, comparing these full-scale transient model runs with corresponding simulations in the scaled, vertically-distorted model domain (Fig. 13) demonstrates that the

formation and evolution of the anti-cyclonic circulation at the entrance to the converging, up-sloping approach to the FBC (over the 700 s model run duration) is qualitatively similar to the oceanic counterpart, both showing a general migration with elapsed time towards the FBC. In this regard, both full-scale and reduced, distorted scale model runs indicate strong temporal variability in predicted outflow pathways and circulations within the WTB/FBC approach, with clear implications for (i) the regulation of volume fluxes through the FBC, (ii) the variability in the WTR overflow strength, and (iii) the overall response of dense water outflow pathways within the Faroese Channels to parametric changes imposed at the FSC inlet boundary. However, this observed variability in the outflow pathways also makes it difficult to determine any clear parametric influences on the circulations generated within the Faroese Channels and/or the degree to which they promote WTR spillage.

In terms of the cross-channel structure of density fields observed within the WTB, it is interesting to note from the field survey by Mauritzen *et al*. (2005), along a similar transect to S1 (see Fig. 2), that the depth measurements of isopycnals were also observed to be strongly time-dependent, experiencing both periods of relative uplift and depression in elevation. Similarly, in full-scale MITgcm simulations of the Faroese Channels, Stashchuk *et al*. (2011) demonstrated an analogous structure in the isotherm elevations across the WTB [after 20 and 30 days, Fig. 14(a), (b)] to that measured along transect S1 in the current scaled laboratory experiments (Fig. 9). Stashchuk *et al*. also noted that the isotherms evolved over time to a more fan-like structure [i.e. after 40 or 50 days, Fig. 15(c), (d)], attributing this behaviour to the generation and evolution of the large anti-cyclonic eddy found in the WTB/FBC channel approach, which was demonstrated to form an opposing current system through the cross-section of the eddy, resulting in the observed lifting and sinking of the isotherms. The presence and evolution of a similar anti-cyclonic circulation has been demonstrated in both

distorted and full scale numerical simulations, as well as in the scaled laboratory experiments and, thus, it seems likely to be the main cause of the undulating and fan-like isopycnal/isotherm structures that are both modelled and observed across the WTB. Furthermore, the observed pinching of isopycnals on the left (WTR) side of the WTB (i.e. transects S1 and S2, Fig. 9) is also in general agreement with previous field survey measurements in the Faroese Channels (*e.g*. Borenäs and Lundberg, 1988; 2004; Mauritzen *et al*., 2005) and the numerical simulations of Stashchuk *et al*. (2011). This wedged-shaped stratification, encountered commonly in the FBC overflow, has been attributed to boundary Ekman dynamics (Johnson and Sanford, 1992) and/or inviscid processes resulting from the presence of an intermediate water mass within the FBC (Borenäs *et al*., 2001).

Acknowledgements

This work was supported by the Natural Environment Research Council (NERC) under the Strategic Ocean Funding Initiative (SOFI) programme. The authors are also grateful for the comments provided by two anonymous reviewers that have led to significant improvements in the paper.

References

Borenäs, K., Lake, I. L. and P. Lundberg (2001). On the Intermediate Water Masses of the Faroe–Bank Channel Overflow. *J. Physical Oceanography*, 31, 1904 – 1914.

Borenäs, K. and Lundberg, P. (1988). On the deep-water flow through the Faroe Bank Channel. *J. Geophys. Res.*, 93(C2), 1281 – 1292.

Borenäs, K. and Lundberg, P. (2004). The Faroe-Bank Channel deep-water overflow. *Deep-Sea Research Part II*, 51, 335-350.

Cuthbertson, A. J. S., Laanearu, J., Wåhlin, A. and Davies, P. A. (2011). Experimental and analytical investigation of dense gravity currents in a rotating, up-sloping and converging channel. *Dynamics of Atmospheres and Oceans*, 52 (3), 386-409.

Cuthbertson, A. J. S., Lundberg, P., Davies, P. A. and Laanearu, J. (2013). Gravity Currents in Rotating, Wedge-Shaped Adverse Channels. *In press: Environ. Fluid Mech.*, DOI 10.1007/s10652-013-9285-4.

Dalziel, S. (2008). Digiflow Users Guide. (http://www.damtp.cam.ac.uk/lab/digiflow).

Davies, P. A., Wåhlin, A. K. and Guo, Y. (2006). Laboratory and Analytical Model Studies of the Faroe Bank Channel Deep-Water Outflow. *J. Phys. Oceanogr.*, 36 (7), 1348-1364.

Ellett, D (1998). Norwegian Sea Deep Water overflow across the Wyville Thomson Ridge during 1987-88. *ICES Cooperative Research Report*, 225, 195-205.

Girton, J. B., L. J. Pratt, D. A. Sutherland and J. F. Price (2006). Is the Faroe Bank Channel overflow hydraulically controlled? *J. Physical Oceanography*, 36, 2340-2349.

Hansen, B. and Østerhus, S. (2000). North Atlantic-Nordic Seas Exchanges. *Progress in Oceanography*, 45, 109-208

Johnson, C, T.J Sherwin, T. Shimmield, & D. Smythe-Wright. (2010). Wyville Thomson Ridge **o**verflow **w**ater: **s**patial and temporal distribution in the Rockall Trough. *Deep Sea Res.***,** 57, 10, 1153-1162

Johnson, G. C. and Sanford, T. B. (1992). Secondary Circulation in the Faroe Bank Channel Overflow, *J. Physical Oceanography*, 22, 927-933.

Laanearu, J. and Lundberg, P. (2003). Topographically constrained deep-water flows in the Baltic Sea. *J. Hydr. Res*., 49(4), 257-265.

Laanearu, J. and Davies, P. (2007). Hydraulic control of two-layer flow in 'quadratic'-type channels. *J. Hydr. Res*., 45, 1, 3-12.

Lake, I., Borenäs, K. and Lundberg, P. (2005). Potential-Vorticity Characteristics of the Faroe Bank Channel Deep-Water Overflow. *J. Physical Oceanography*, 35, 921-932.

Marshall, J., Adcroft, A., Hill, C., Perelman, L. and Heisey, C. (1997). A finite-volume, incompressible Navier-Stokes model for studies of the ocean on parallel computers. *J. Geophys. Res.*, 102, 5733-5752.

Mauritzen, C., Price, J., Sanford, T. and Torres, D. (2005). Circulation and mixing in the Faroese Channels. *Deep-Sea Research Part I*, 52, 883-913.

Murray, J (1886). The physical and biological conditions of the seas and estuaries about north Britain. *Proc. Phil. Soc. Glasgow*, 306 – 333

Olsen, S.M, Hansen, B., Quadfasel, D & Østerhus, S. (2008). Observed and modelled stability of overflow across the Greenland Scotland ridge. *Nature*, 455, 519-522.

Orlanski, I. (1976). A simple boundary condition for unbounded hyperbolic flows. *J. Comp. Phys*, 21 (3), 251-269.

Pratt, L. J., Helfrich, K., and Chassingnet, E. P. (2000). Hydraulic adjustment to an obstacle in a rotating channel. *J. Fluid Mech.*, 404, 117-149.

Saunders, P (1990). Cold outflow from the Faroe Bank Channel. *J. Phys. Oceanogr*., 20, 29-43.

Sherwin, T.J. and Turrell, W.R.. (2005). Mixing and advection of a cold water cascade over the Wyville Thomson Ridge. *Deep Sea Res*., I, 52, 1392-1413.

Sherwin, T. J., Williams, M. O., Turrell, W. R., Hughes, S. L. and Miller, P. I. (2006). A description and analysis of mesoscale variability in the Faroe-Sheltand Channel. *J. Geophys. Res.*, 111, C03003.

Sherwin, T. J., Griffiths, C.R., Inall, M.E. & Turrell, W.R. (2008). Quantifying the overflow across the Wyville Thomson Ridge into the Rockall Trough. *Deep Sea Res*., 55, 4, 396-404

Stashchuk, N., Vlasenko, V. and Sherwin, T. (2010). Insights into the structure of the Wyville Thomson Ridge overflow current from a fine-scale numerical model. *Deep-Sea Res. I*, 57, 1192-1205.

Stashchuk, N., Vlasenko, V. and Sherwin, T. (2011). Numerical investigation of deep water circulation in the Faroese Channels. *Deep-Sea Res. I*, 58, 787-799.

van Heijst, G. J. F., Davies, P.A. and Davis, R. G. (1990). Spin up in a rectangular container. *Phys. Fluids*, A2, 150-159

Whitehead, J A (1998). Topographic control of oceanic flows in deep passages and straits. *Reviews of Geophysics*, 36, 3, 423-440.

Wåhlin, A.K. (2002). Topographic steering of dense bottom currents with application to submarine canyons. *Deep-Sea Res.*, 49(2), 305–320.

Figure Captions

Fig. 1: Overview maps showing main seabed topographic features of the Faroese Channels, including: Faroe-Shetland Channel (FSC); Wyville-Thomson Basin (WTB); Wyville-Thomson Ridge (WTR); Faroe Bank (FB); Faroe Bank Channel (FBC); Ellet Gully (EG); Ymir Ridge (YR); Cirolana Deep (CD); Rockall Trough (RT). Detailed seabed topography enclosed by dashed rectangle in (a) shown in (b), along with the main Norwegian Sea Deep Water (NSDW) outflow pathways (blue arrows) through the FBC and across the WTR.

Fig. 2: Transformed and scaled seabed topography used in the laboratory model set-up, with model inlet and outlet boundary locations highlighted. Colour bar scale indicates the height (cm) above the lowest bed elevation ($z_{b,min} = 0$) in the topographic model. Micro-conductivity probe measurement transects S1 – S3 shown along with MITgcm WTB transect (dotted white line) also shown. Note: abbreviations for prominent seabed features as detailed in Fig. 1 caption.

Fig. 3: (a) Contour-layered construction of topographic model of Faroese Channels showing abbreviations for prominent seabed features (as detailed in Fig. 1 caption); (b) photograph showing dye-tracing experimental set-up, where fluorescene-dyed dense bottom water flowing through the smoothed topography is illuminated by an ambient light source. (Insert defined this bottom water layer thickness h_1 and interface width l_1 at FSC inlet boundary).

Fig. 4: Dense bottom water overflow pathways observed through illuminated fluorescene dye-tracing for Run 1 conditions (see Table 1) with Bu_1: Q_1^* values of (a) 0.124: 0.00352 (no WTR spill), (b) 0.116: 0.00528 (WTR spill), (c) 0.114: 0.00704 (WTR spill) and (d) 0.115: 0.00915 (WTR spill).

Fig. 5: (a) Relationship between non-dimensional transport parameter Q_1^* and the inlet Burger number Bu_1 showing parametric conditions under which WTR spill and no spill occur, (b) regime diagram of Q_1^* versus non-dimensional inlet length ratio h_1/l_1 indicting

delineation between spill and no-spill conditions. Typical adjusted estimates of Q_1^* , Bu_1 and h_1/l_1 values for the full-scale, deep-water inflow conditions in the FSC are shown for comparison.

Fig. 6: Typical drogue tracking for dense water outflow layer in Faroese Channels region under investigation for runs with Bu_1: Q_1^* values of (a-b) 0.363: 1.9×10^{-4} (Run 3b, Table 1); (c-d) 0.202: 1.26×10^{-3} (Run 2c); (e-f) 0.114: 5.99×10^{-3} (Run 5c); (g-h) 0.110: 4.49×10^{-3} (Run 5b). Time step between plotted drogue positions Δt = 0.42 s (every 10 image frames @ 24 fps). Background images show fluorescene-dyed overflow pathways for equivalent runs.

Fig. 7: Typical drogue tracks showing circulation paths in dense water overflow in the converging, up-sloping approach to the FBC sill. Plots (a-c) show 18 drogue trajectories in the WTB/FBC approach for Run 6b (Table 1) with Bu_1: Q_1^* values of 0.199: 8.7×10^{-4}. Time step between plotted drogue positions Δt = 0.42 s. Background images show fluorescene-dyed overflow pathways for equivalent run.

Fig. 8: Schematic representation of dense water outflow pathways from drogue tracking measurements. Solid and dashed lines represent main and secondary pathways, respectively. Shaded areas show main regions where vorticity (+ve and –ve) was observed. Note: abbreviations for prominent seabed features as detailed in Fig. 1 caption.

Fig. 9: Cross-channel isopycnal (ρ' = 0.1 – 0.9) elevations at transects S1 – S3 (see Fig. 2 for transect locations) for the parametric conditions specified in (a) Run 1 and (b) Run 3 (see Table 1). The specific pycnocline plots shown at each transect are for Bu_1: Q_1^* values of (a)(i) 0.115: 9.15×10^{-3} (Run 1d), (a)(ii) 0.124: 3.52×10^{-3} (Run 1a), (b)(i) 0.343: 3.4×10^{-4} (Run 3d) and (b)(ii) 0.368: 1.3×10^{-4} (Run 3a).

Fig. 10: Comparison of MITgcm-predicted (left) and measured (right) dyed bottom water traces through Faroese channel topography for Bu_1: Q_1^* values of (a) 0.363: 0.00019 (Run 3b, Table 1); (b) 0.202: 0.00126 (Run 2c); and (c) 0.199: 0.00087 (Run 6b). Colour scale on

numerical predictions represents tracer concentration (0% – initial basin concentration; 100% – undiluted deep water tracer concentration at the FSC inlet boundary).

Fig. 11: MITgcm predictions of velocity vector fields at 20cm and 25cm depths for Bu_1: Q_1^* values of (a) 0.363: 0.00019 (Run 3b, Table 1); (b) 0.202: 0.00126 (Run 2c); (c) 0.199: 0.00087 (Run 6b); (d) 0.114: 0.00599 (Run 5c); and (e) 0.110: 0.00449 (Run 5b). Velocity vector scales as shown in Figure.

Fig. 12: MITgcm-predicted temporal evolution of the density field across WTB transect (dotted white line, Fig. 2) for Bu_1: Q_1^* values of (a) 0.110: 0.00449 (Run 5b, Table 1) and (b) 0.114: 0.00599 (Run 5c). Colour scale represents water density ρ (kg/m^3).

Fig. 13: MITgcm-predicted evolution in the velocity field at the depth of the scaled WTR ridge depression (20 cm) for Bu_1: Q_1^* values of 0.110: 0.00449 (Run 5b, Table 1). Greyscale bar represents depth (m) and velocity vector scale as shown.

Fig. 14: Full-scale MITgcm simulations of the thermocline development at the WTB transect (dotted white line, Fig. 2) after 20, 30, 40 and 50 days (taken from Stashchuk et al., 2011). Temperature contours shown are in °C

Table Captions

Table 1: Main experimental parameters for scaled laboratory model runs

Figure 1

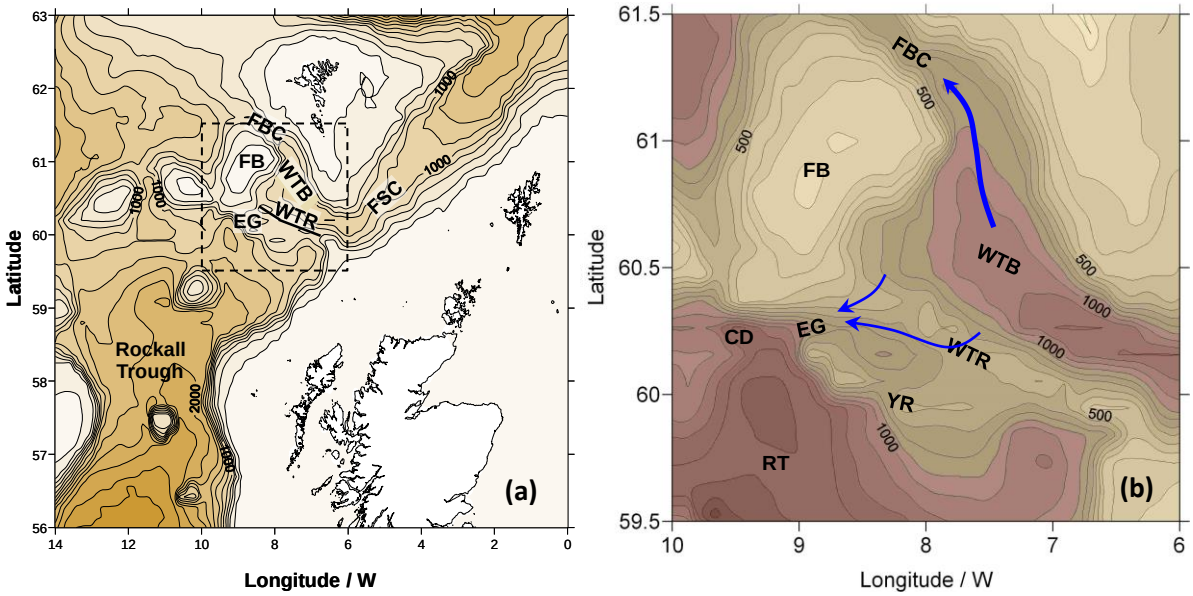
Latitude
Longitude / W
FBC
FB
WTB
FSC
EG
WTR
Rockall
Trough
2000
1000
500
(a)
(b)
CD
YR
RT

Figure 2

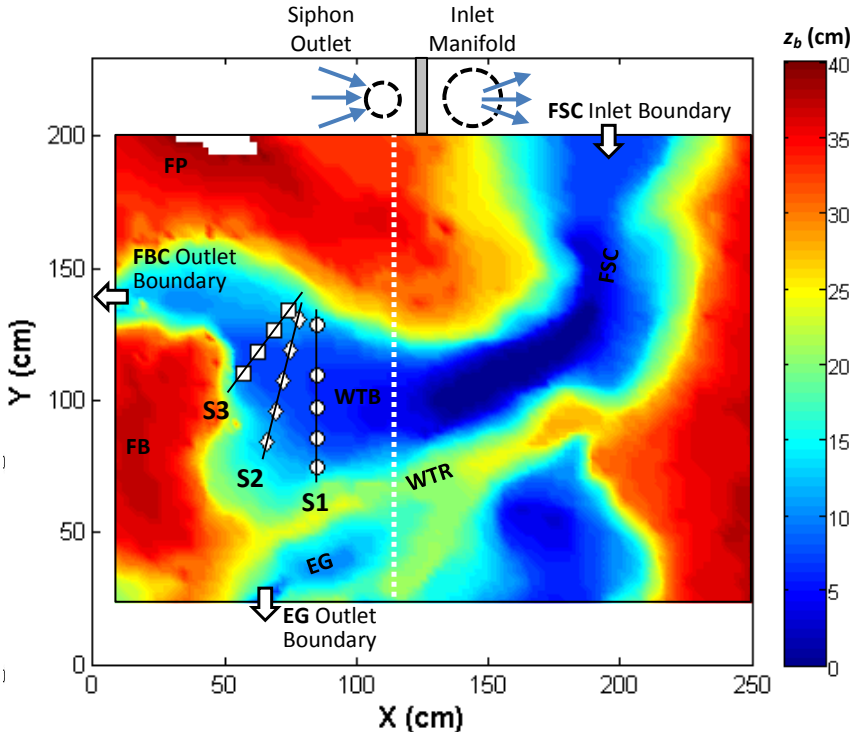
Siphon Outlet
Inlet Manifold
FSC Inlet Boundary
FP
FBC Outlet Boundary
FSC
WTB
S3
FB
S2
S1
WTR
EG
EG Outlet Boundary
Y (cm)
X (cm)
z_b (cm)
0
50
100
150
200
250
0
5
10
15
20
25
30
35
40

Figure 3

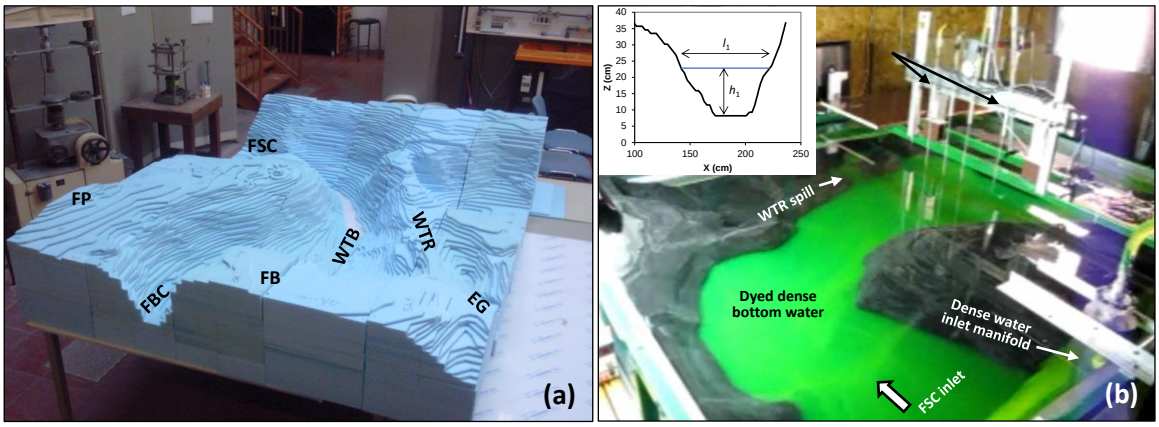
FSC
FP
WTB
WTR
FB
FBC
EG
(a)
Z (cm)
X (cm)
l_1
h_1
WTR spill
Dyed dense
bottom water
Dense water
inlet manifold
FSC inlet
(b)

Figure 4

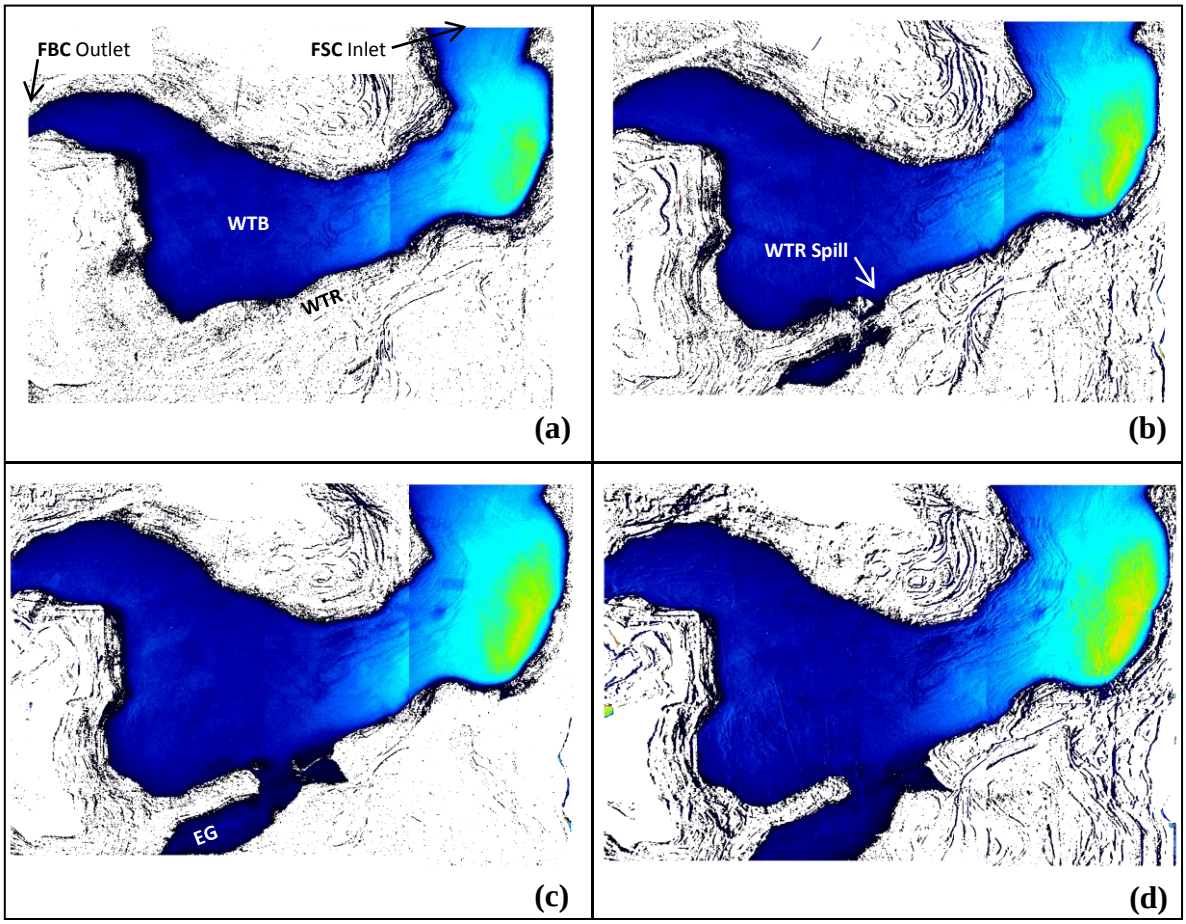

Figure 5

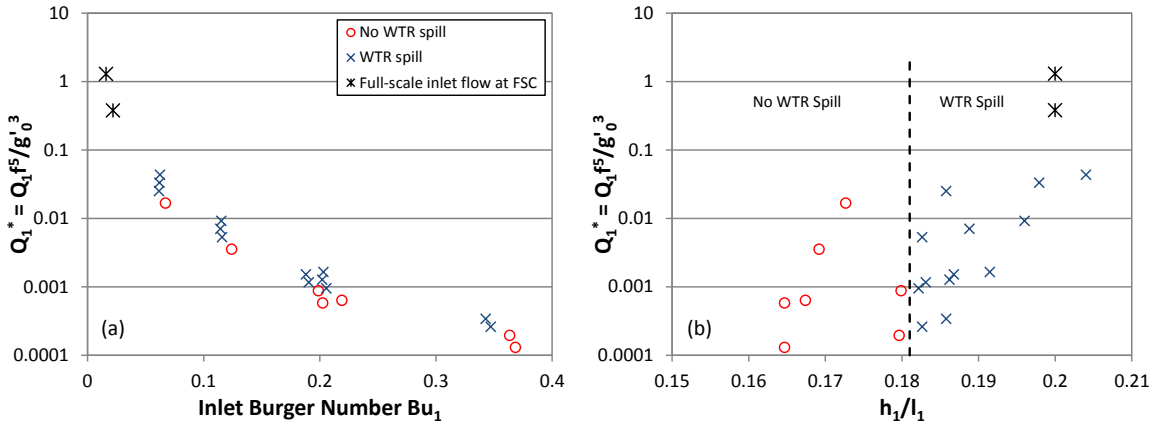
No WTR spill
WTR spill
Full-scale inlet flow at FSC
(a)
Inlet Burger Number Bu1
No WTR Spill
WTR Spill
(b)
h1/l1

Figure 6

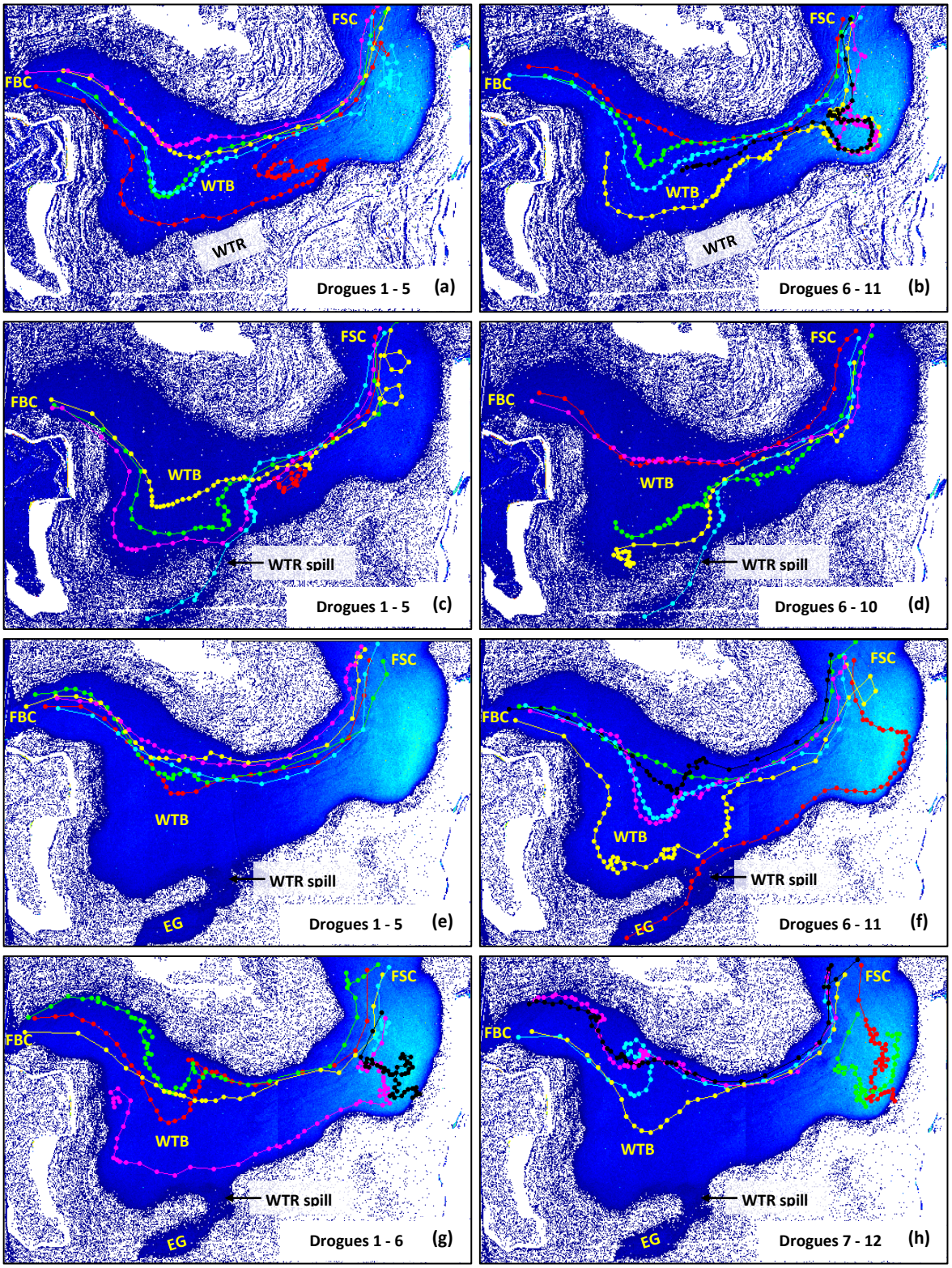
FSC
FBC
WTB
WTR
Drogues 1 - 5
(a)
FSC
FBC
WTB
WTR
Drogues 6 - 11
(b)
FSC
FBC
WTB
WTR spill
Drogues 1 - 5
(c)
FSC
FBC
WTB
WTR spill
Drogues 6 - 10
(d)
FSC
FBC
WTB
WTR spill
EG
Drogues 1 - 5
(e)
FSC
FBC
WTB
WTR spill
EG
Drogues 6 - 11
(f)
FSC
FBC
WTB
WTR spill
EG
Drogues 1 - 6
(g)
FSC
FBC
WTB
WTR spill
EG
Drogues 7 - 12
(h)

Figure 7

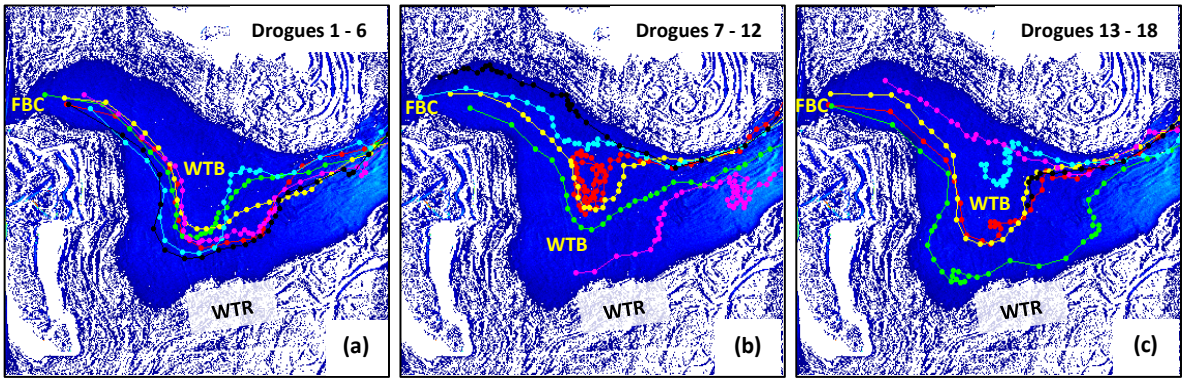
Drogues 1 - 6
FBC
WTB
WTR
(a)
Drogues 7 - 12
FBC
WTB
WTR
(b)
Drogues 13 - 18
FBC
WTB
WTR
(c)

Figure 8

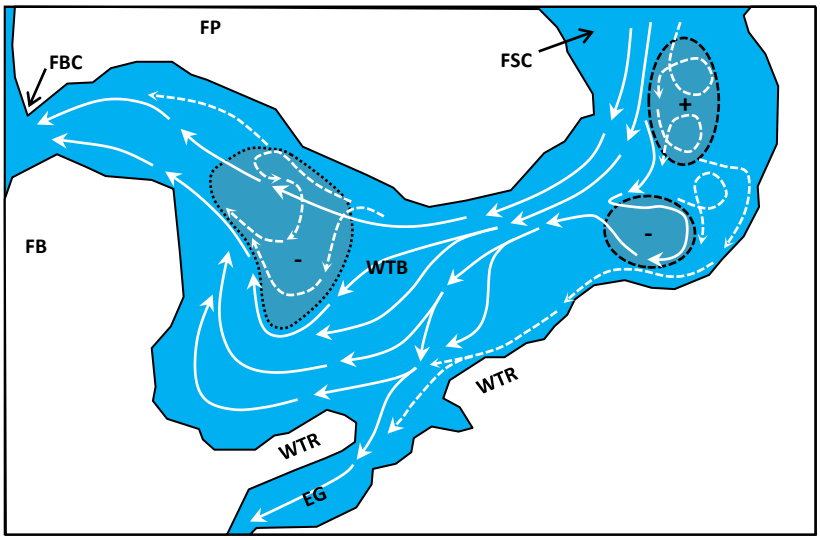

Figure 9

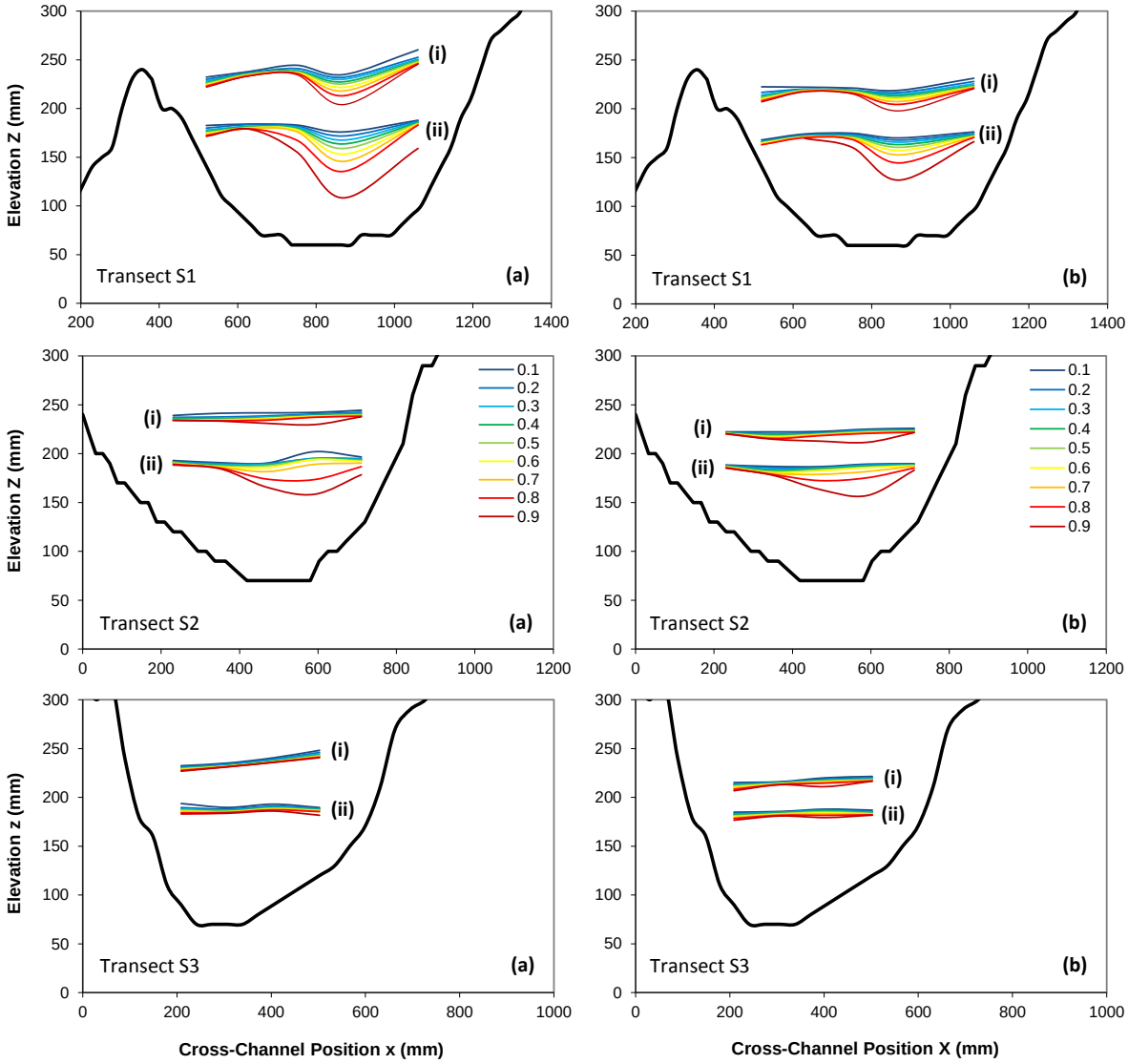
Elevation Z (mm)
Transect S1
(a)
(i)
(ii)
Transect S1
(b)
Elevation Z (mm)
Transect S2
(a)
0.1
0.2
0.3
0.4
0.5
0.6
0.7
0.8
0.9
Transect S2
(b)
Elevation z (mm)
Transect S3
(a)
Cross-Channel Position x (mm)
Transect S3
(b)
Cross-Channel Position X (mm)

Figure 10

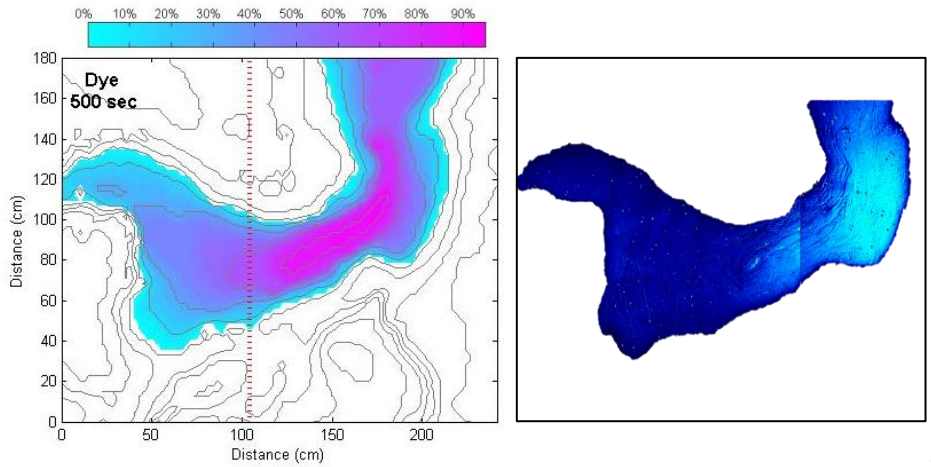

(a)

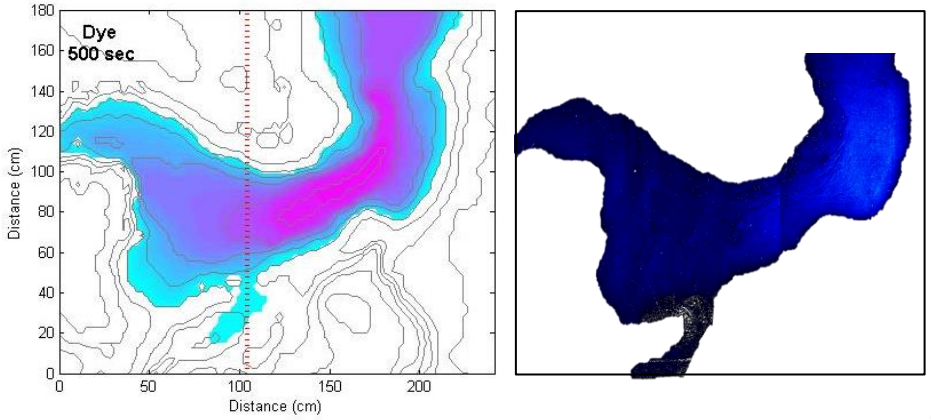

(b)

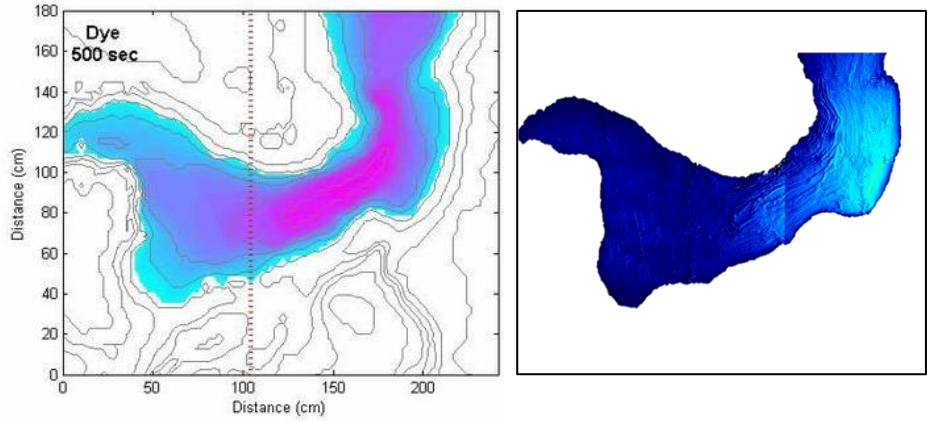

(c)

Figure 11

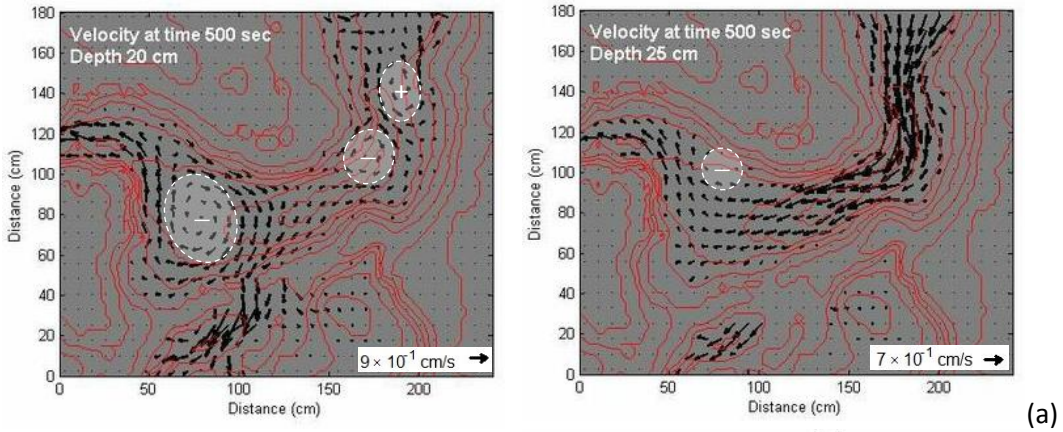

(a)

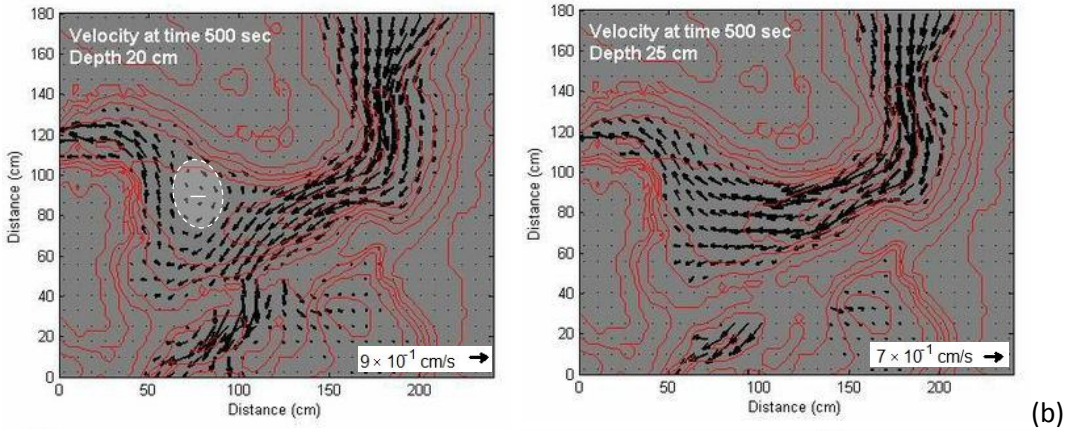

(b)

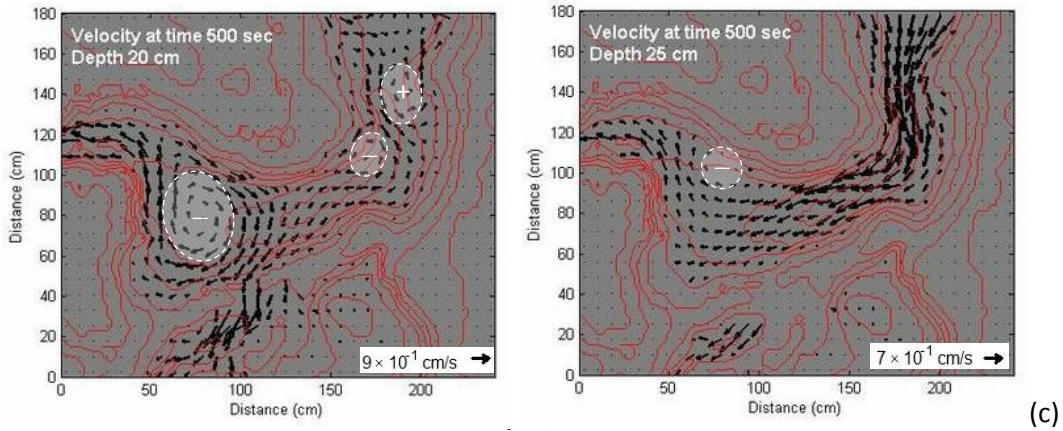

(c)

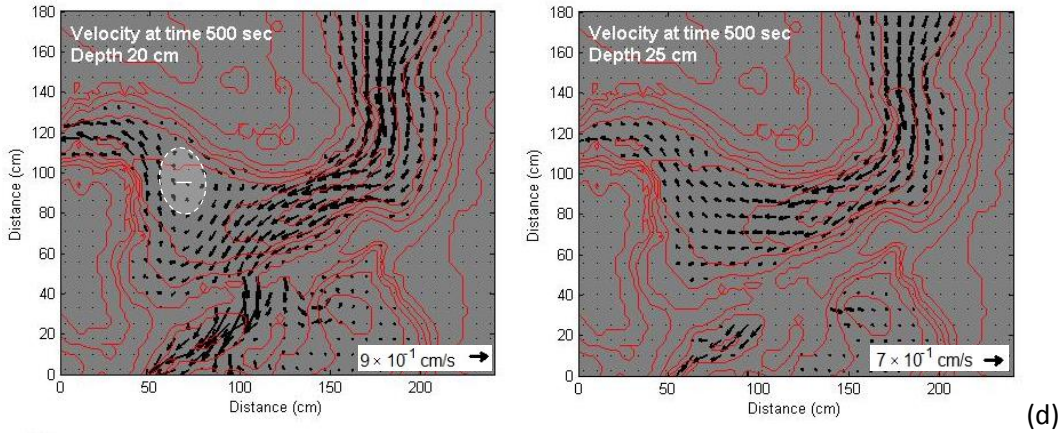

(d)

Figure 11 cont/d

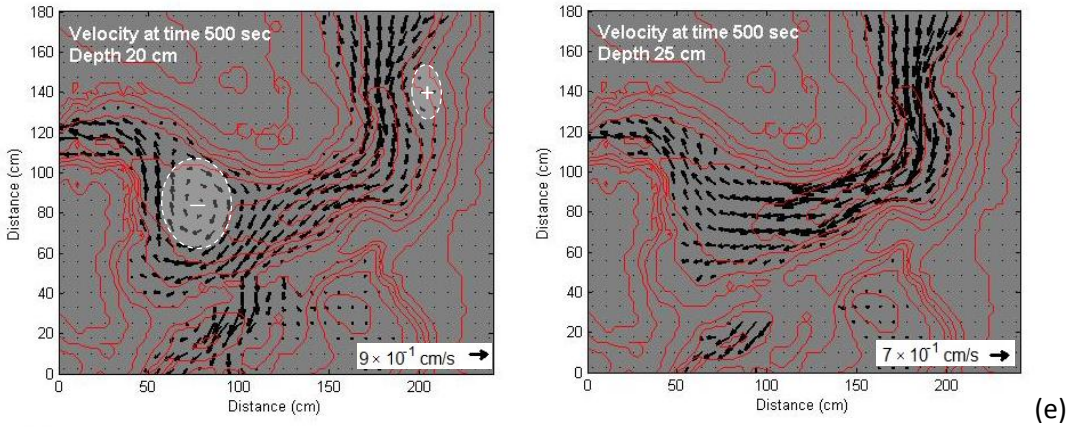

(e)

Figure 12

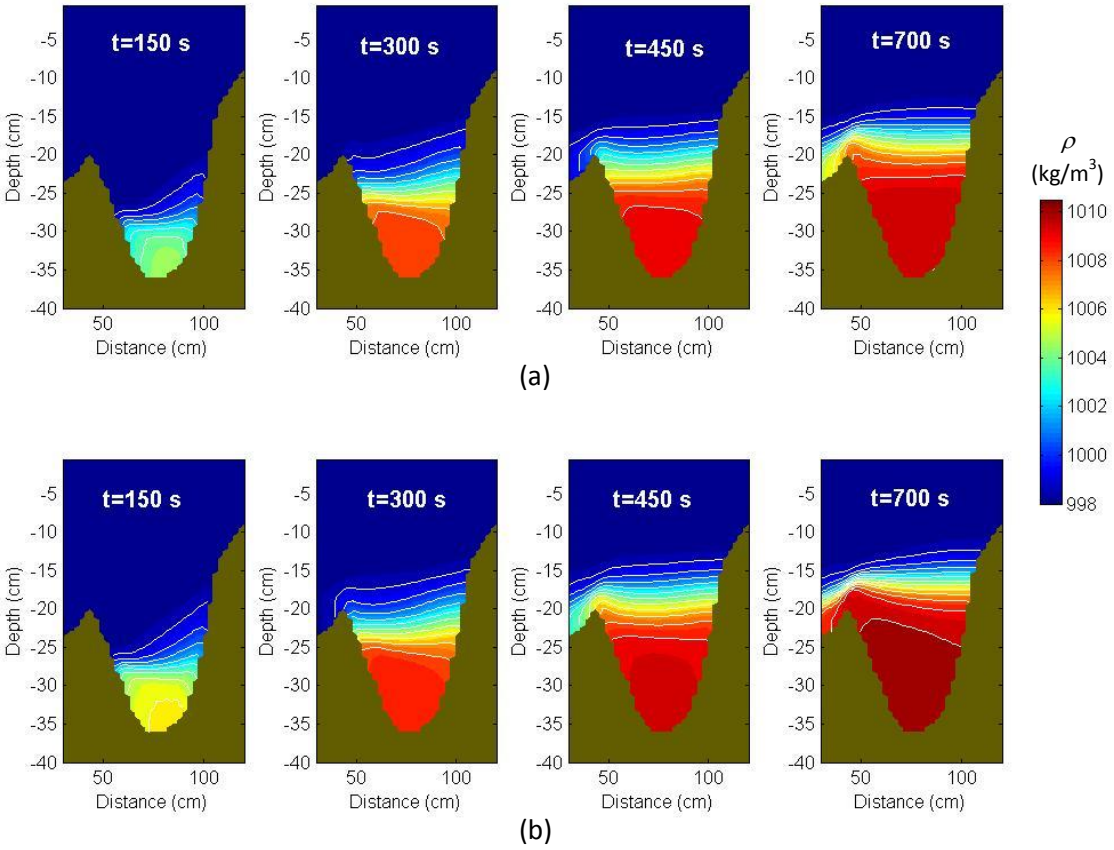
t=150 s
t=300 s
t=450 s
t=700 s
Depth (cm)
Distance (cm)
(a)
(b)
ρ
(kg/m3)
1010
1008
1006
1004
1002
1000
998

Figure 13

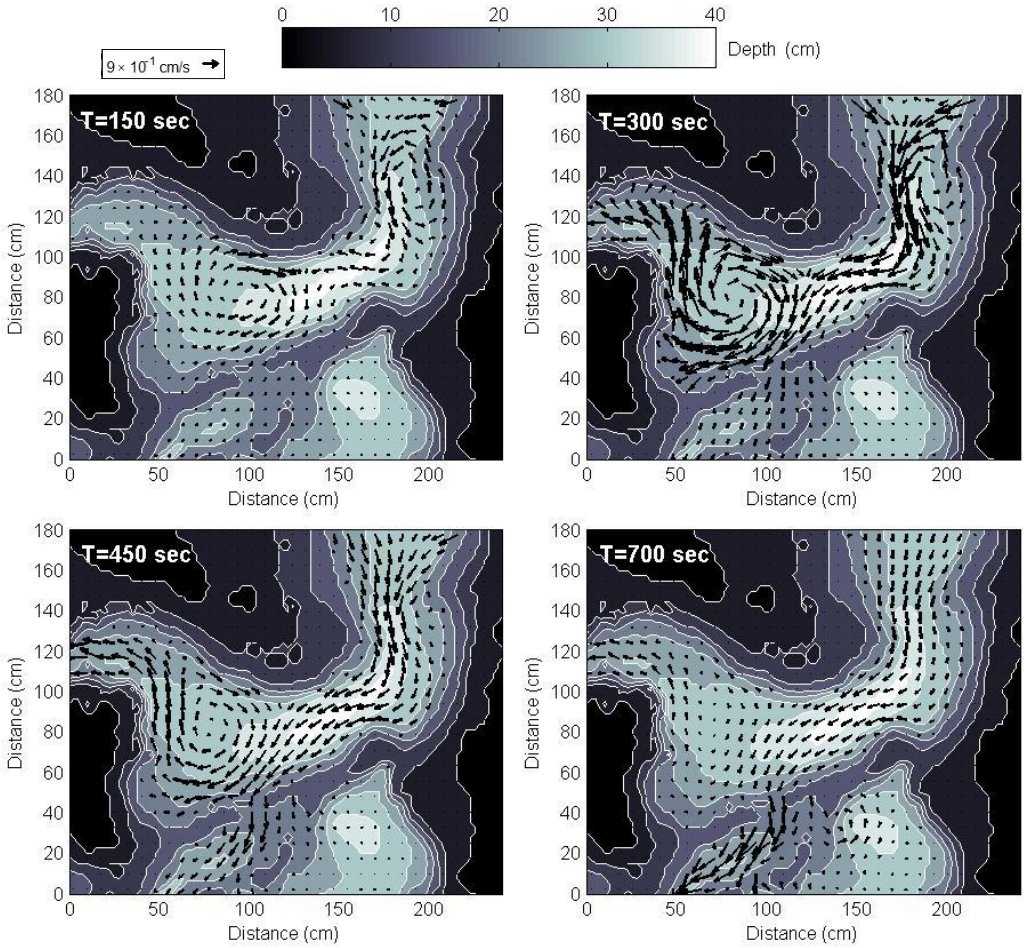
0
10
20
30
40
Depth (cm)
9 × 10-1 cm/s
T=150 sec
T=300 sec
T=450 sec
T=700 sec
Distance (cm)
Distance (cm)
0
20
40
60
80
100
120
140
160
180
0
50
100
150
200

Figure 14

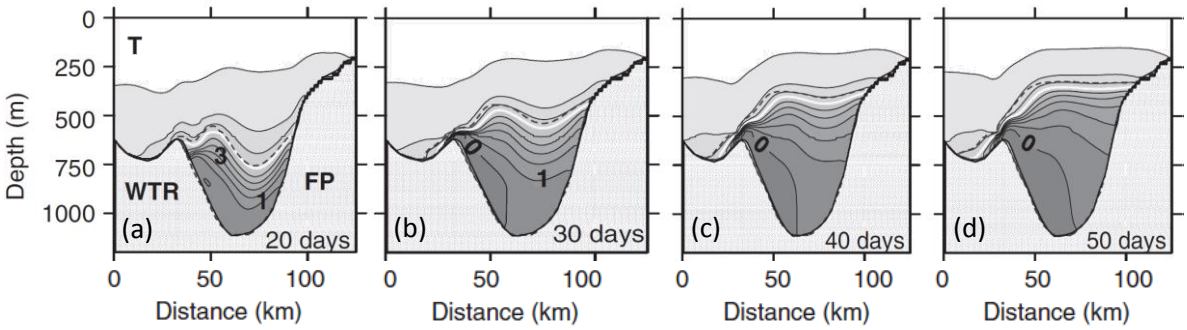
Depth (m)
0
250
500
750
1000
T
WTR
FP
3
1
(a)
20 days
0
1
(b)
30 days
0
(c)
40 days
0
(d)
50 days
0
50
100
Distance (km)

Table 1: Main experimental parameters for scaled laboratory model

Run No.		ρ_0 (kg.m^{-3})	ρ_1 (kg.m^{-3})	g' (m.s^{-2})	T_r (s)	f (s^{-1})	Q_1 (l.min^{-1})	h_1 (m)	l_1 (m)	F_1 ($\times 10^{-2}$)	Ro_1 ($\times 10^{-2}$)	Bu_1	Re_1 ($\times 10^3$)	Q_1^* (= $Q_1 f^5/g'$)
1 (1),(3)	a	998	1005	0.068	34.0	0.370	10	0.117	0.689	3.23	1.14	0.124	1.351	0.00352
	b						15	0.146	0.797	3.17	1.08	0.116*	1.846	0.00528*
	c						20	0.158	0.834	3.61	1.22	0.114*	2.374	0.00704*
	d						26	0.169	0.860	4.11	1.40	0.115*	2.989	0.00915*
2 (1),(2),(3)	a	998	1010.5	0.121	34.0	0.370	10	0.115	0.684	2.51	1.17	0.219	1.368	0.00063
	b						15	0.145	0.793	2.41	1.09	0.206*	1.862	0.00095*
	c						20	0.154	0.824	2.85	1.28	0.202*	2.416	0.00126*
	d						26	0.162	0.843	3.36	1.51	0.203*	3.067	0.00164*
3 (1),(2),(3)	a	998	1019.5	0.207	34.0	0.370	10	0.112	0.677	2.02	1.23	0.368	1.394	0.00013
	b						15	0.135	0.749	2.12	1.28	0.363	1.938	0.00019
	c						20	0.146	0.797	2.43	1.43	0.347*	2.497	0.00026*
	d						26	0.153	0.821	2.88	1.68	0.343*	3.178	0.00034*
4 (1),(2),(3)	a	998	1005	0.068	25.0	0.502	10	0.121	0.698	3.03	0.79	0.067	1.333	0.01660
	b						15	0.153	0.821	2.89	0.72	0.061*	1.807	0.02490*
	c						20	0.172	0.867	3.05	0.76	0.062*	2.279	0.03320*
	d						26	0.182	0.890	3.55	0.89	0.062*	2.881	0.04315*
5 (2),(3)	a	998	1010.5	0.121	25.0	0.502	10	0.114	0.733	2.50	0.81	0.105	1.373	0.00299
	b						15	0.140	0.793	2.53	0.84	0.110	1.892	0.00449
	c						20	0.152	0.820	2.87	0.97	0.114	2.431	0.00599
	d						26	0.158	0.834	3.46	1.17	0.114	3.105	0.00779
6 (1),(2),(3)	a	998	1019.5	0.207	25.0	0.502	10	0.112	0.677	2.02	0.91	0.203	1.394	0.00058
	b						15	0.136	0.753	2.09	0.93	0.199	1.932	0.00087
	c						20	0.147	0.800	2.39	1.05	0.191*	2.489	0.00116*
	d						26	0.155	0.827	2.80	1.22	0.188*	3.159	0.00151*

(1) Dye tracing experiments; (2) Drogue tracking experiments; (3) Density profiling experiments

* [Bu_1: Q_1*] parametric conditions under which WTR spillage occurs (dye tracing runs only)

Experimental runs simulated by MITgcm: 2b; 3c; 5b; 5c; 6b